Title
Nanosecond Laser Assisted Fabrication of Large Area Metallic Nanostructures and Their Potential Applications

Author
Xiao, Fan

Publication Date
2015

Peer reviewed|Thesis/dissertation

UNIVERSITY OF CALIFORNIA

Los Angeles

Nanosecond Laser Assisted Fabrication of Large Area Metallic Nanostructures and Their Potential Applications

A dissertation submitted in partial satisfaction of the requirements for the degree Doctor of Philosophy in Mechanical Engineering

by

Fan Xiao

2015

ABSTRACT OF THE DISSERTATION

Nanosecond Laser Assisted Fabrication of

Large Area Metallic Nanostructures

and Their Potential Applications

by

Fan Xiao

Doctor of Philosophy in Mechanical Engineering

University of California, Los Angeles, 2015

Professor Pei-Yu Chiou, Chair

Techniques for processing nanoscale metallic and semiconductor structures with spatial order and tunable physical characteristics, such as size and shape, are important for realizing broad applications in areas such as magnetism, optics, electronics, biosensing, and drug delivery. Laser annealing is widely applied in modern semiconductor manufacturing processes for crystallizing amorphous structures into polycrystalline structures using thermal energy from laser illumination. This project aims to develop nanosecond laser assisted photothermal annealing technologies for high throughput nanofabrication of metal nanostructures on both planar and nonplanar surfaces using pulse laser induced rapid heating and nanomorphology evolution processes. This technology allows direct printing/transfer of functional devices on rigid

substrates such as glass, silicon, as well as on flexible, low melting temperature substrates such as plastic and polymer. By controlling optical patterns through means of using phase-shifting photomask or pre-patterning the metal film to take advantage of the structured substrate, as well as selecting desired laser illumination duration, light wavelength, pulse number and dosage energy, thermal energy can be selectively deposited at target locations to melt materials within that area followed by nanomorphology evolution driven by surface tension. Such a low cost, high throughput and high spatial resolution nanofabrication technology could provide numerous applications in various areas including photonic devices, nanoelectronics, bio/chemical sensors, and devices for improved energy capturing and conversion in large area.

We further developed a novel gold nanoparticle embedded PDMS micropillar array to measure cell force in a large scale. The gold nanoparticles serve as point source like scattering hot spots in dark field images, where PDMS pillars and cells are almost invisible. By fitting the gold nanoparticle image with Gaussian point spread function, 30 nm pillar localization precision could be achieved even using a low N.A. 20x objective lens. This precision is comparable to prior reported fluorescent pillars imaged by a high magnification optical system with 60x or 100x objective lenses. Our plasmonic pillar sensor allows for monitoring collective cell behavior in a much larger area without sacrificing the force resolution. The plasmonic pillar also has the potential for directly delivering molecules into live cells through transient holes on the cell membrane opened by rapidly expanding cavitation bubbles, which are photothermally generated by gold nanoparticles sitting on pillar tip under laser triggering pulses.

The dissertation of Fan Xiao is approved.

Greg Carman

Hsian-Rong Tseng

Yong Chen

Pei-Yu Chiou, Committee Chair

University of California, Los Angeles

2015

DEDICATION

For my family, Zan and Blake Zhang.

CONTENTS

LIST OF FIGURES

ACKNOWLEDGEMENTS

First of all, I would like to thank Professor Pei-Yu Chiou for his guidance on my research and continuous support throughout my study during past seven years. He is always very encouraging and caring for student. Without his help, I couldn't have enjoyed my PhD life as I did. I would like to thank Professor Greg Carman, Professor Hsian-Rong Tseng and Professor Yong Chen for their service on my thesis committee.

I also would like to thank Dr. Ting-Hsiang Wu for being my mentor ever since I joined this lab. She shared all her experience with me in building optical system, operating lasers and designing experiments. Many thanks go to Dr. Yi-Chien Wu, Dr. Ming-Yu Lin, Yu-Chun Kung, Ximiao Wen, Yajia Yang, and Xiongfeng Zhu, who are always available to help and discuss with me in every aspect of my experiments. I would like to thank all other former and current members of Optofluidics Systems Laboratory for their help in my research and their lasting friendship.

Finally, special gratitude goes to my mom and my parents-in-law for being so supportive in my life. Love to my husband for his unfaltering support and belief in me throughout all my ups and downs. To my son, thank you for coming to my world. Your smile means everything to me. Mom love you so much.

VITA

2008 B. S., Microelectronics
Peking University
Beijing, China

PUBLICATIONS AND PRESENTATIONS

Xiao F., Wen X., Chiou P. Y., "Gold Nanoparticle embedded PDMS micropillar array for large area cell force sensing", Photofluidics 2015, Jul 2015.

Xiao F., Wu T.-H., Chiou P. Y., "Near field photothermal printing of gold microstructures and nanostructures", Applied Physics Letter, Vol 97, pp. 031112, 2010.

Xiao F., Chiou P. Y., "Reshaping Gold Micro and Nano Structures with Polarization Dependent Photothermal Annealing", IEEE/LEOS International Conference on Optical MEMS and Nanophotonics, pp. 1-2, Aug 2010.

Xiao F., Wu T.-H., Chiou P. Y., "Near Field Photothermal Annealing for Rapid Laser Printing of Metallic Micro and Nano Structures", in Proceeding of Solid-State Sensor, Actuator, and Microsystems Workshop (Hilton Head '10), pp.1-4, June 2010

Wu T.-H., Xiao F., Teitell M. A., Chiou P. Y., "Molecular delivery into live cells using gold nanoparticle coated substrates fabricated by pulsed laser annealing", SPIE Photonics West BioS, San Francisco, CA, pp.1-7, January 2010.

Wu T.-H., Xiao F., Kalim S., Teslaa T., Teitell M. A., Chiou P. Y., "Molecular delivery into live cells using gold nanoparticle arrays fabricated by polymer mold guided near-field photothermal annealing", ASME 2010 First Global Congress on NanoEngineering for Medicine and Biology, Houston, TX, pp. 1-2, February 2010.

Chapter 1

Introduction

Techniques for processing nanoscale metallic and semiconductor structures with spatial order and tunable physical characteristics, such as size and shape, are important for realizing broad applications in areas such as magnetism, optics, electronic, biosensing, and drug delivery. Laser annealing is widely applied in modern semiconductor manufacturing processes for crystallizing amorphous structures into polycrystalline structures using thermal energy from laser illumination. This project aims to develop a nanosecond laser assisted photothermal annealing technology for high throughput nanofabrication of metal nanostructures on both planar and nonplanar surfaces using pulse laser induced rapid heating and nanomorphology evolution processes as illustrated in Fig. 1.1. This technology allows direct printing/transfer of functional devices on both rigid substrates such as glass, silicon and on flexible, low melting temperature substrates such as plastic and polymer.

To achieve desired spatial arrangement of metallic nanostructures, two approaches are usually utilized, redistributed optical energy deposition on continuous metal film[1-3] or flood

exposure on pre-patterned metal film[4-6]. In the former category, Nishioka[1] *et al*. proposed to use a linearly polarized laser beam since periodic energy density distribution can be formed spontaneously on the metal surface due to interference between the incident beam and a scattered surface wave from the substrate. The redistributed optical energy will selectively melt the metal in highest density area. The molten metal will migrate to adjacent cold area where the optical density is not sufficient to melt the material. However, the contrast between the maximum and minimum energy density is low, hundred pulses are needed to gradually finish film cutting. In order to form a sharply redistributed optical energy, multiple beam interference lithography[2, 3] is used. The laser is spilt into two or four beams and reconstructed on metal film to fabricate grating and mesh structures. This process takes only one to few pulses. However, these structures are usually limited to periodic structures, whose periodicity depends on laser wavelength and incident angle. Our near field photothermal printing technique falls in this regime. By controlling optical patterns by means of using phase-shifting photomask, as well as selecting desired laser illumination duration, light wavelength, pulse number and dosage energy, thermal energy can be selectively deposited in target locations to melt materials within that area followed by nanomorphology evolution driven by surface tension. With properly designed photomasks, both periodic and arbitrary metallic structures can be accomplished.

Fabrication of gold nanoparticle array on structured substrates, such as PDMS micropillar array, can be achieved by laser induced transfer. During morphology change of molten metal, excess surface energy is converted to kinetic energy which results in strong upward motion of the material, during which gold nanodroplets depart one substrate and get transferred to another one. Gold nanoparticles transferred to PDMS substrate are found embedded in the pillar tip. Such plasmonic pillar array is used to measure cell force in a large scale. These gold nanoparticles

serve as point source like scattering hot spots under dark field imaging mode, where the scattering signals from the PDMS pillars and cells are almost invisible. By fitting the gold nanoparticles image with Gaussian point spread function, 30 nm localization precision could be achieved even by using a 20x objective lens. This precision is comparable to elsewhere reported fluorescent pillars when imaged by a highly magnified optical system with 60x or 100x objective lenses. Our plasmonic pillar sensor allows for monitoring collective cell behavior in a much larger area without sacrificing the force resolution. The plasmonic pillar also has potential for directly delivering molecules into live cells through transient holes on the cell membrane opened by rapidly expanding cavitation bubbles, which are photothermally generated by gold nanoparticles sitting on pillar tip under laser triggering pulses.

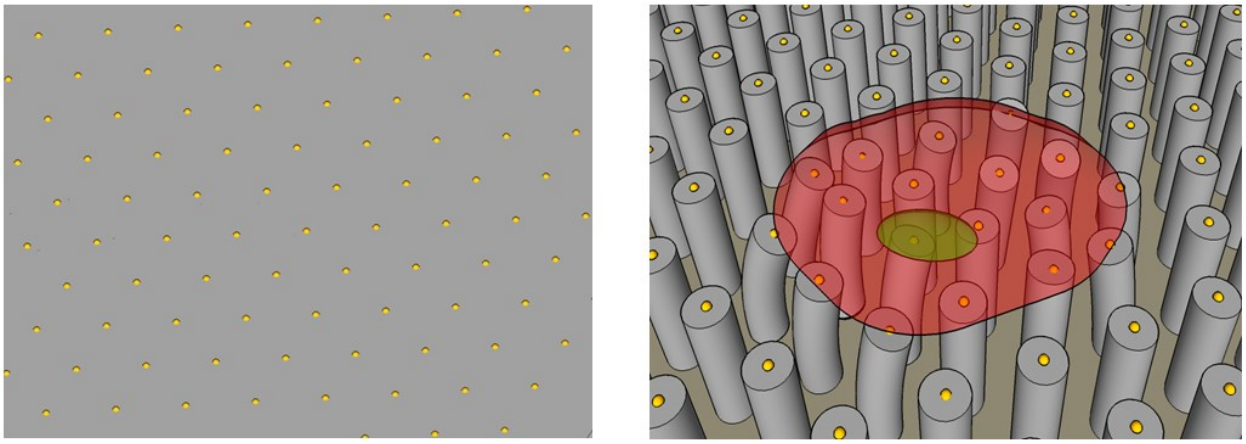

Figure 1.1 Schematic of fabrication of large area metallic nanostructures on flat and structured substrates.

Chapter 2

Photothermal Printing of Metallic Micro and Nano Structures

2.1 Introduction to near field photothermal printing of metal

Metallic micro and nanostructures have wide applications in solar cell harvesting[7], plasmonic devices[8], color filters[9], biomedical fields such as metallic particle guided gene delivery[10], photothermal therapy[11], and biosensors[12]. Methods for fabricating metallic nanostructures are versatile, ranging from chemical synthesis[13], electron beam or focused ion beam lithography[14], nanoimprint lithography[15], nanosphere lithography[16], to template-assisted deposition[17], and laser induced dewetting processes[1]. Among them, laser induced dewetting process is considered as an economical method for rapid and large area fabrication. Laser beam irritates on thin metal film which is normally deposited on dielectric substrates, and strongly gets absorbed by metal. Due to photothermal effect, optical energy converts into thermal energy, resulting in a variety of physical process in metal including melting and evaporation. Hydrodynamic self-redistribution of metal can be realized if there are distinctly adjacent molten

and un-molten zones determined by the incident laser fluence in the local area. Molten metal can migrate to un-molten zones driven by surface tension and re-texture the morphology of metal film.

To guide laser induced dewetting and self-organization processes, two types of methods have been proposed, using pre-patterned metal films or spatially shaping the projected laser patterns. Multi-beam Interference Lithography (MIL) belongs to the latter type and allows low cost and rapid fabrication of two-dimensional nanostructures on a continuous thin metallic film as shown in Fig. 2.1. Using nanosecond laser pulses, MIL based photothermal annealing techniques are capable of direct laser printing of periodic metallic nanostructures from thin metal films coated on various types of substrates including glass, silicon, and polymer. However, MIL is limited to fabricating periodic structures with simple shapes.

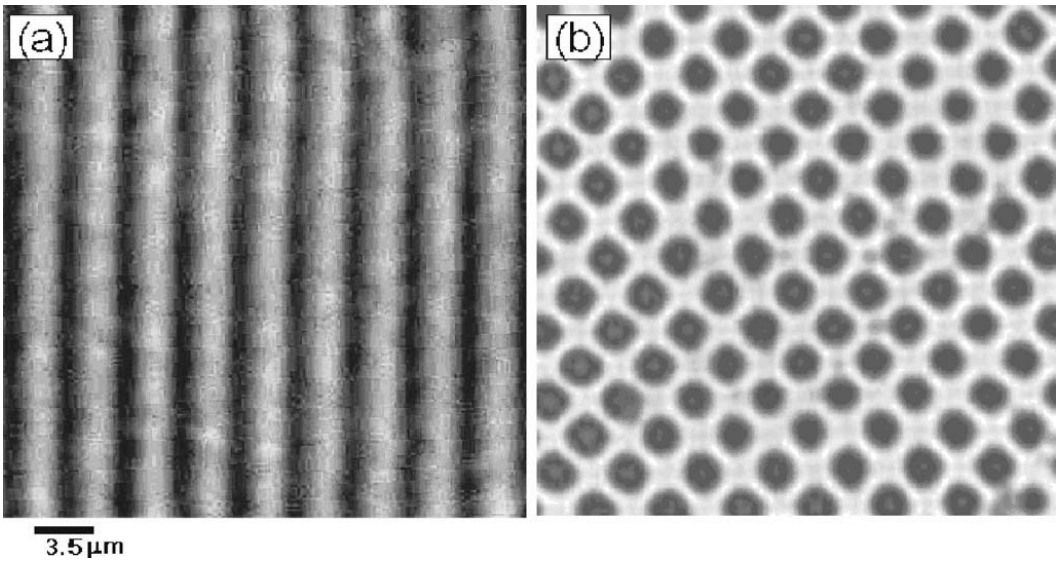

Figure 2.1 Optical micrographs of (a) one-dimensional and (b) two-dimensional gratings created on a gold film of 18 nm thickness by MIL. Adapted from Ref. 2.

Here, we propose a rapid laser printing technology capable of fabricating both periodic and non-periodic metallic structures using near field photothermal annealing guided by a transparent phase-shifting mask as illustrated in Fig. 2.2. A laser pulse with uniform spatial light intensity passing through a PDMS phase-shifting mask redistributes its optical energy in space and forms a non-uniform light intensity profile at the interface of this PDMS mask and the underlying gold thin film. The laser pulses shaped by the PDMS phase-shifting mask selectively heat up and melt the gold film in areas with high light intensity. Due to instability of a molten gold film on a glass substrate, the molten film, driven by surface tension, quickly migrates to cold areas. The shape evolution of the molten film is controlled by surface tension of molten gold, laser pulse energy, duration, and pulse number. Furthermore, since the local shape of a PDMS mold determines the near field light pattern, NPTP has the potential for fabricating arbitrary shape 2D metal nanostructures by designing the PDMS phase-shifting mask.

Single step of photothermal annealing finishes within hundreds of nanosecond, as illustrated in Fig. 2.3. Noble metal has a large amount of free electrons. In nanoscale, these free electrons dominate the optical properties of metal through the phenomenon called surface plasmon, which is the collective oscillation of free electrons on the metal surface. When external electromagnetic wave comes in with a frequency close to these electrons oscillation frequencies, strong absorption occurs. These absorbed energy converts into lattice heat in few picoseconds and rapidly heats up the metal. Melting happens within few nanoseconds and lasts hundred nanoseconds in case of a nanosecond laser pulse. The material quickly redistributes during the melting state, and eventually cools down and solidifies. Since the formation of these gold nanostructures needs only one to few laser pulses, it has the potential for rapid, large-scale nanofabrication by scanning laser pulses across a large area.

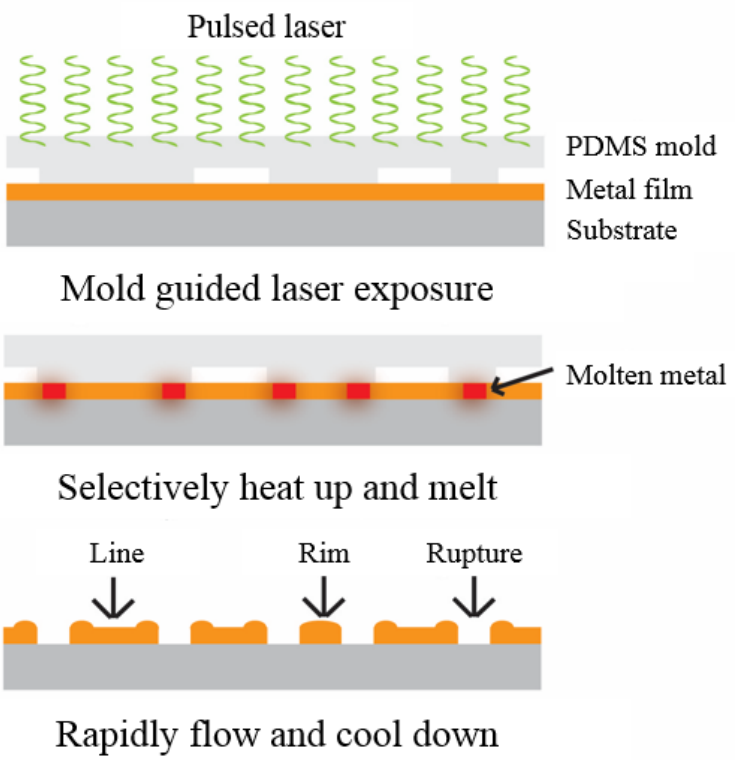

Figure 2.2 Schematic of phase shifting mask guided printing of metal film under collimated laser pulse irradiation.

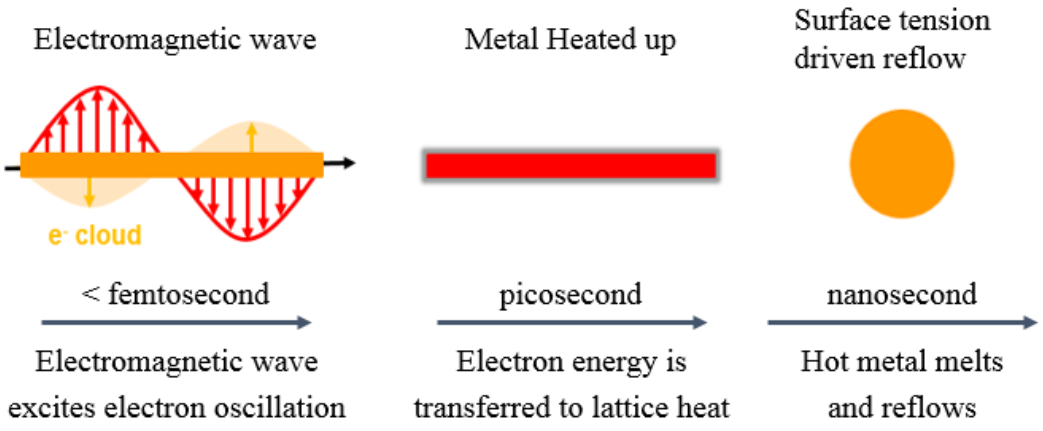

Figure 2.3 Time scale of surface plasmon enhanced photothermal effect in metal.

2.2 Simulation and experiment

Phase shifting mask, also called mold, plays a key role in photothermal printing by determining the redistributed spatial intensity of optical energy. Both periodic and non-periodic metallic structures can be obtained by properly designed masks. In experiment, we employ commercially available plane ruled reflection or diffraction grating to replicate periodic PDMS mold and home-design arbitrary PDMS mold.

To quantitatively analyze the photothermal effect, a three-step approach is usually used. First, the optical energy redistributed across the whole scope, including mold, metal film and substrate, at the excitation laser wavelength is calculated. Secondly, optical absorption in the metal film, which gives rise to heating and melting of metal, is derived. The absorption is characterized by the imaginary part of the dielectric function of metal at that specific excitation wavelength. Finally, temperature distribution in metal film can be obtained by solving a heat transfer equation with a heat generation term that is assumed to be 100% converted from the absorbed optical energy. In this work, we focus on the phase shifting effect of the mold on redistributing laser optical energy, therefore only the first step is analyzed.

In the experiment, a Q-switched, frequency doubled Nd:YAG pulse laser (Minilite I, Continuum) with a pulse width of 6 ns and wavelength of 532 nm is applied. Energy before entering the PDMS mold is tuned by a set of half-wavelength plate and polarization dependent beam-splitter. A 1 nm titanium/10 nm gold thin film is deposited by means of electron beam evaporation on a thin cover glass substrate. Titanium is necessary here to promote adhesion between gold film and glass substrate. The PDMS mold is gently put in contact with gold film

with no pressure applied. The annealing result is examined by optical microscope and scanning electron microscope (SEM).

Periodic structure

Periodic PDMS mold is simply fabricated by replicating the plane ruled reflection or diffraction grating (Newport Corp) with periodicity ranging from 1 to 10/3 μm, as shown in Fig. 2.4. The grating is treated with silane to facilitate the later separation from PDMS mold. Uncured PDMS (Poly-dimethylsiloxance, Sylgard 184, Dow Corning) with a ratio of 10 base: 1 curing agent is vacuumed for half an hour in a vacuum chamber and then poured on a pre-cleaned thin glass slide. Grating is transferred onto PDMS and pressed down with figures to squeeze out bubbles trapped in PDMS. After PDMS is cured at 65°C for at least 4 hours, the grating is carefully lifted off from PDMS/glass side and redundant PDMS around replicated grating structure area is removed by a razor blade.

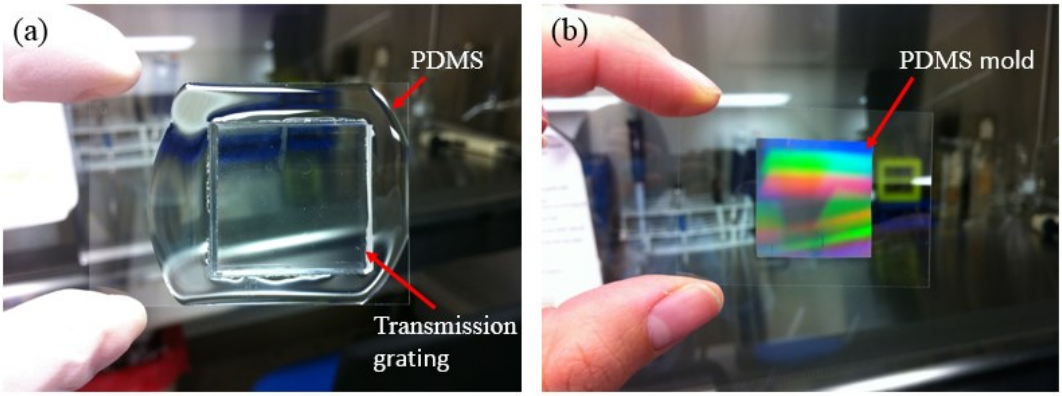

Figure 2.4 Fabrication of PDMS mold from a transmission grating. (a) Before grating is separated from cured PDMS; (b) Finished look of PDMS mold.

Fig. 2.5 shows the simulated light intensity distribution near a periodic PDMS mold and a gold thin film using the finite difference time domain (FDTD) method (FullWAVE, RSoft Design Group). The incident light is TE polarized with a wavelength of 532 nm. Fig. 2.5(a) shows a PDMS grating mold with 5/3 μm periodicity and ideal cross section of isosceles right triangle shape positioned in contact with a 10 nm gold film on a glass substrate. Fig. 2.5(b) shows electric field redistribution during EM wave propagating through the grating structure. The total energy intensity distribution on the metal surface is plotted in Fig. 2.5(c), which reveals distinct high and low intensity areas. By adjusting the pulse energy, gold in strong light intensity regions is melted and migrates to the adjacent cold areas.

With sufficient laser energy, the continuous film breaks right under the peak of the grating and molten gold flows into empty space between grating peaks where the gold remains solid, forming one-dimensional microwire array. By rotating the PDMS mold by 90° and followed by another few laser pulses, gold wires are cut into two-dimensional microsquare array. Fig. 2.6 shows gold microwire and microsquare array formed by laser pulses with a fluence of 80 mJ/cm^2 using a 10/3 μm periodic PDMS mold.

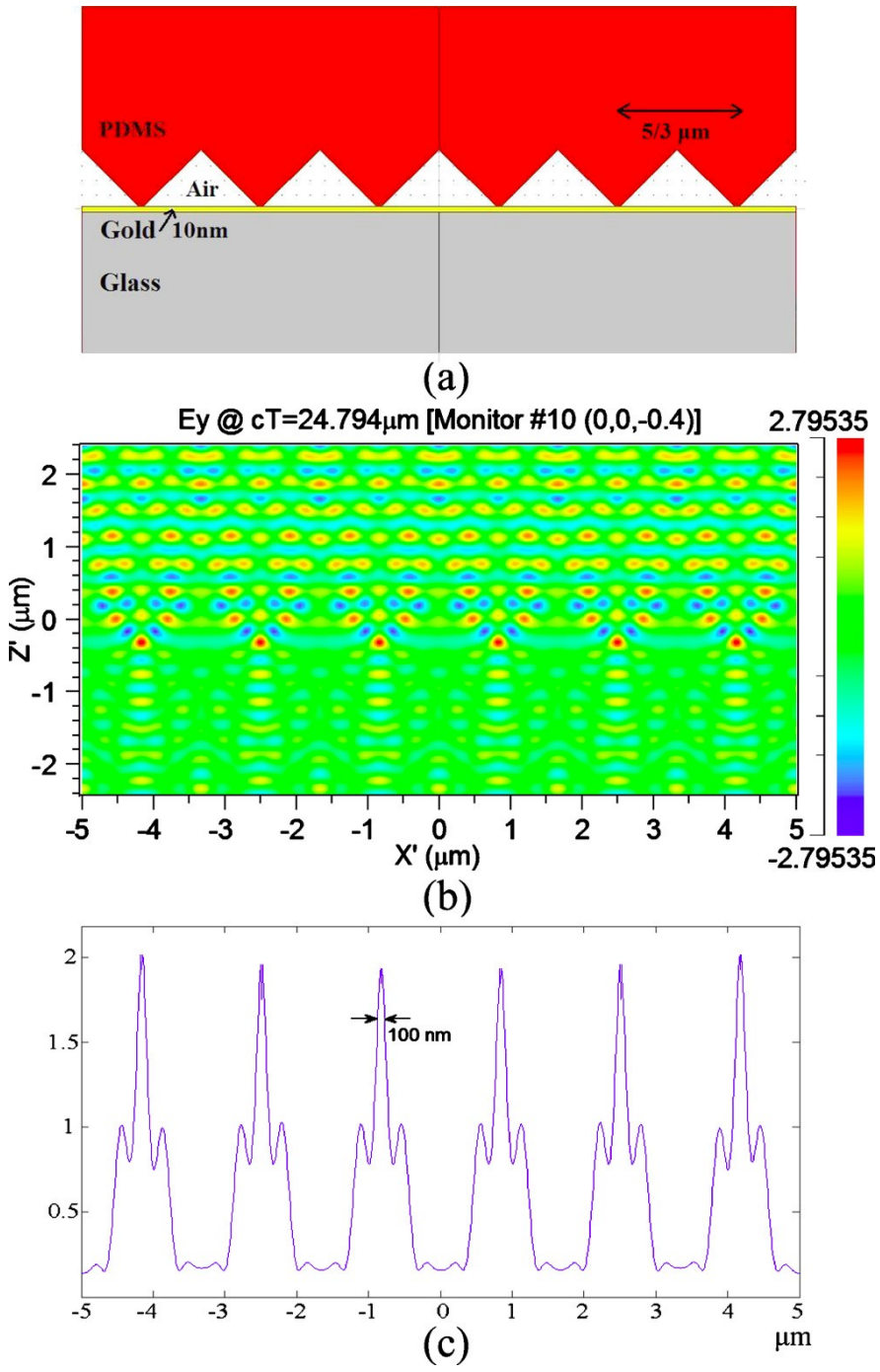

Figure 2.5 Numerical simulation of light intensity redistribution by PDMS mold. (a) Schematic of a phase-shifting PDMS mold and a gold thin film coated substrate used in simulation; (b) Diagram of electrical field distribution; (c) Energy intensity redistribution on gold surface.

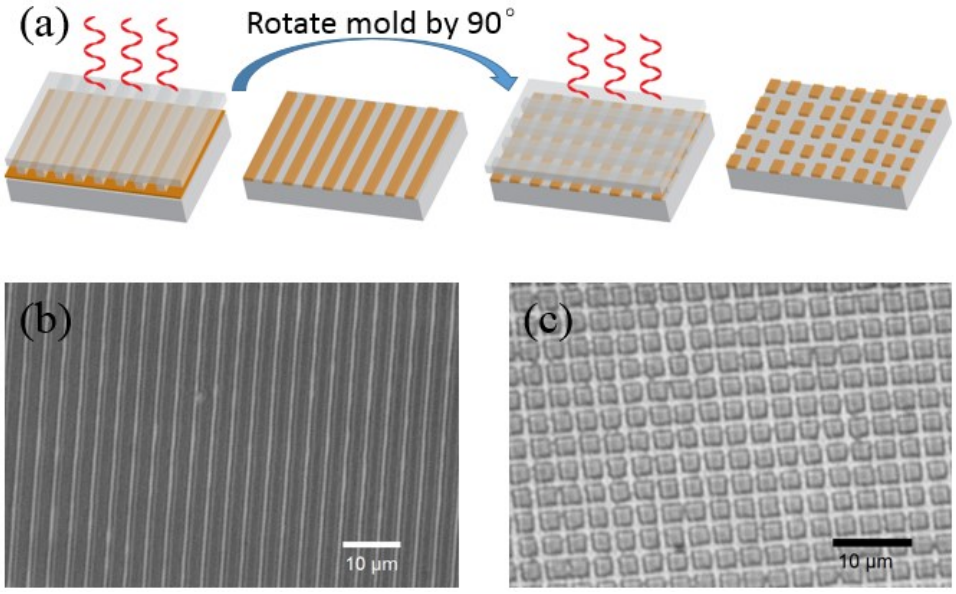

Figure 2.6 Formation of one- and two-dimensional periodic gold structures. (a) Schematic of the process; (b) Formation of microwire array; (c) Formation of microsquare array.

Arbitrary structure

Since this photothermal annealing technique utilizes near field optical patterns to generate local heating to induce metal dewetting, the fabricated structures are not limited to periodic patterns. Any arbitrary shape of patterns can be fabricated by properly designing the phase shifting mask. Fig. 2.7 demonstrates photothermal annealing of few example patterns. The self-designed mold structures are first patterned in photoresist AZ-5214E (MicroChemicals) by photolithography, which serves as a master mold for fabricating the PDMS phase-shifting mask. All patterns are achieved by a single laser pulse with a fluence of 80 mJ/cm^2. With self-designed PDMS phase-shift mask, holes, rings, triangles, crosses, squares, meshes, and more complex shapes can be achieved.

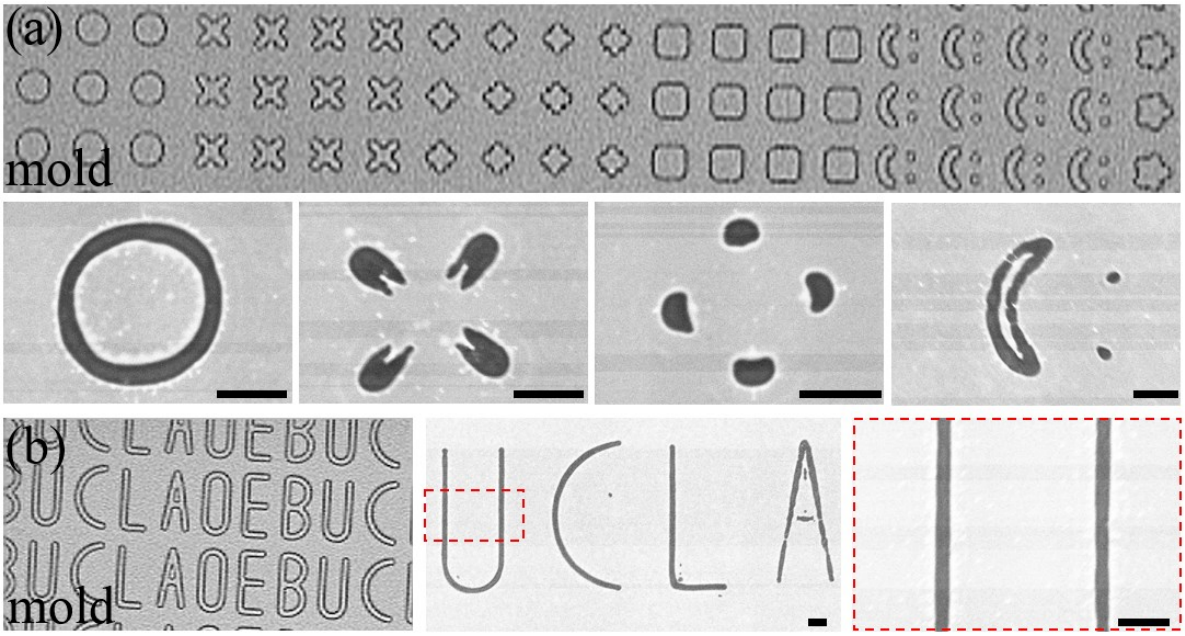

Figure 2.7 Self-designed arbitrary PDMS phase shifting mask and photothermally annealed gold structure by using such PDMS mold. (a) Design of arbitrary shape; (b) Design of characters. Area in dashed red line is enlarged showing annealed line width of 1μm. The scale bar is 5μm.

2.3 Polarization dependent reshaping of metallic structures

Flood exposure can further photothermally reshape the as-fabricated gold structures, which has been reported to anneal prismatic gold nanoparticles into nanospheres by femtosecond laser pulses[4]. This morphology evolution process is polarization dependent as illustrated by Fig. 2.8. Laser pulses with uniform light intensity illuminate on these pre-patterned metallic structures on a glass or silicon substrate. Due to collective electron oscillations in these metallic structures, surface plasmon waves induce strong field enhancement on structure edges. The kinetic energy of these oscillating electrons quickly converts into lattice heat and initiates metal melting in high intensity regions. The molten gold migrates to the cold areas due to surface

tension before cools down. The field enhancement is not uniform along the edge. Edges perpendicular to the laser polarization direction are enhanced most. Shape fine-tuning of metallic nanostructures can be achieved by controlling the pulse energy, numbers, and polarization.

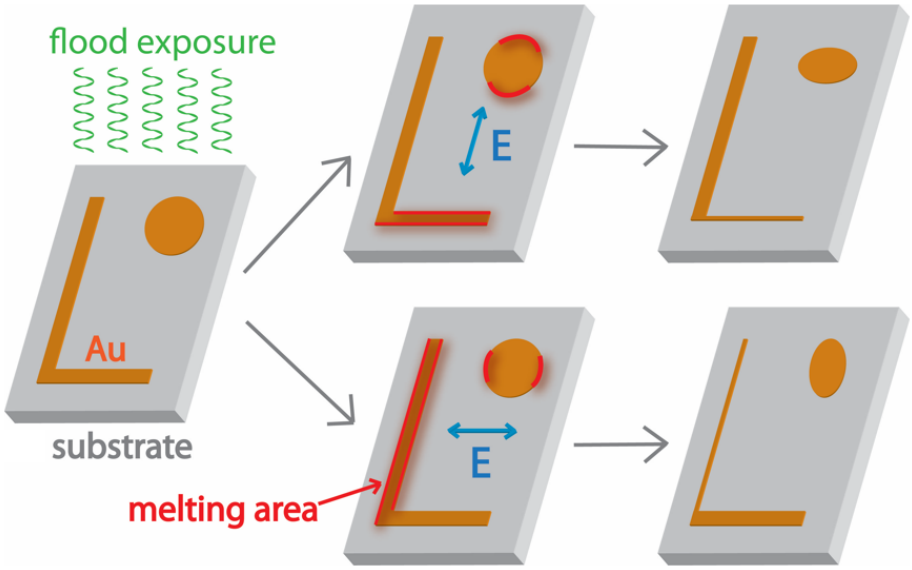

Figure 2.8 Schematic of the working principle of polarization dependent photothermal annealing for fine-tuning the shape of metallic micro and nano structures.

Simulation

Light intensity distribution in a 100 nm thick, 2 μm wide, and 4 μm long rectangular gold structure is simulated using FDTD in Fig. 2.9. Normal incident plane waves with wavelength at 532 nm and electrical field polarization along the short and long axes of the rectangular disks are applied in this simulation. The results indicate that, for both cases, the strong electric energy density occurs at the corners and on the edges perpendicular to the polarization of incident light, predicting stronger photothermal effect in such areas where the melting is initiated.

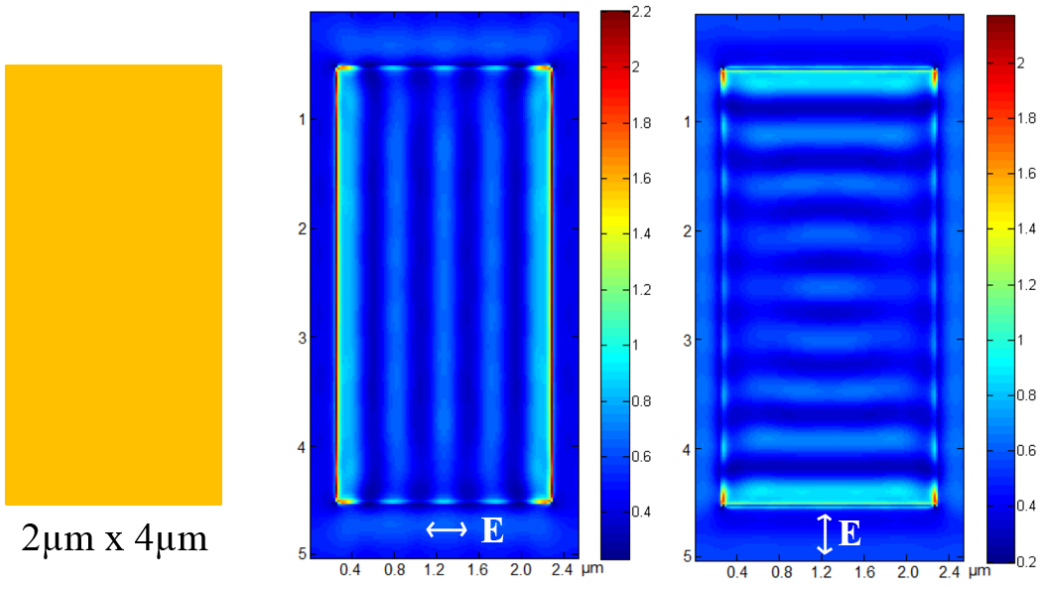

Figure 2.9 FDTD simulation showing the electric energy density distribution under light illumination with different E field polarization.

Experiment

In the experiment, a Q-switched Nd:YAG pulse laser with a pulse width of 6 ns and wavelength of 532 nm is used. 5 nm titanium/100 nm gold microstructures pre-patterned on Si substrate by standard photolithography and lift-off approach are first used. Silicon substrate other than glass is chosen here to better demonstrate the shape evolution for two reasons. First, silicon has larger thermal conductivity than glass, which helps prevent thin metal from evaporation or destructive dewetting due to excessive heat accumulation in intensity peak area of a non-ideal laser beam. Secondly, metal has better adhesion to silicon than glass, which assists reflow of molten gold in smoother motion. Fig. 2.10 demonstrates reshaping of simple microscale structures by flood exposure.

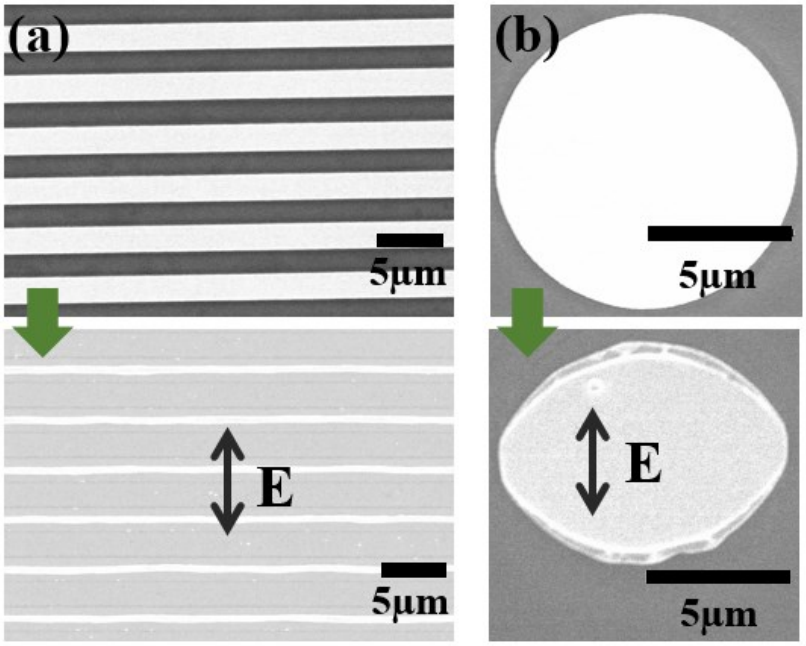

Figure 2.10 Reshaping of simple microscale structures by flood exposure. (a) Micron wires are shaped to sub-micro wires; (b) Circular disk evolves into elliptical shape with short axis along laser polarization direction.

Final shape of metal structure strongly depends on electrical field polarization of incident laser, laser pulse energy and number of these laser pulses. Fig. 2.11 gives more aspects of this characteristic. By flood exposing the patterns under light pulses with different polarization as indicated in Fig. 2.11(a), size reduction occurs in different parts of the initial patterns as predicted by the simulation, which is stronger photothermal effect occurring in edges perpendicular to the polarization of light. Enlarged letter "L" shows that the initial 2 μm wide gold wire evolves into a 400 nm nanowire after flood exposure, while the width of the wire parallel to the field polarization remains almost unchanged. In some cases, electrical field is evenly enhanced on all edges of a pattern, resulting in uniform size reduction across the whole structure. Example is given in Fig. 2.11(b), where the laser beam is polarized 45° with respect to

the axis of a cross. Fig. 2.11(c) evinces the number of pluses will affect the final shape. The reshaping effect gets amplified with reduced dimension, so with more pulses, the center part of the bowtie evolves faster than other areas away from the center.

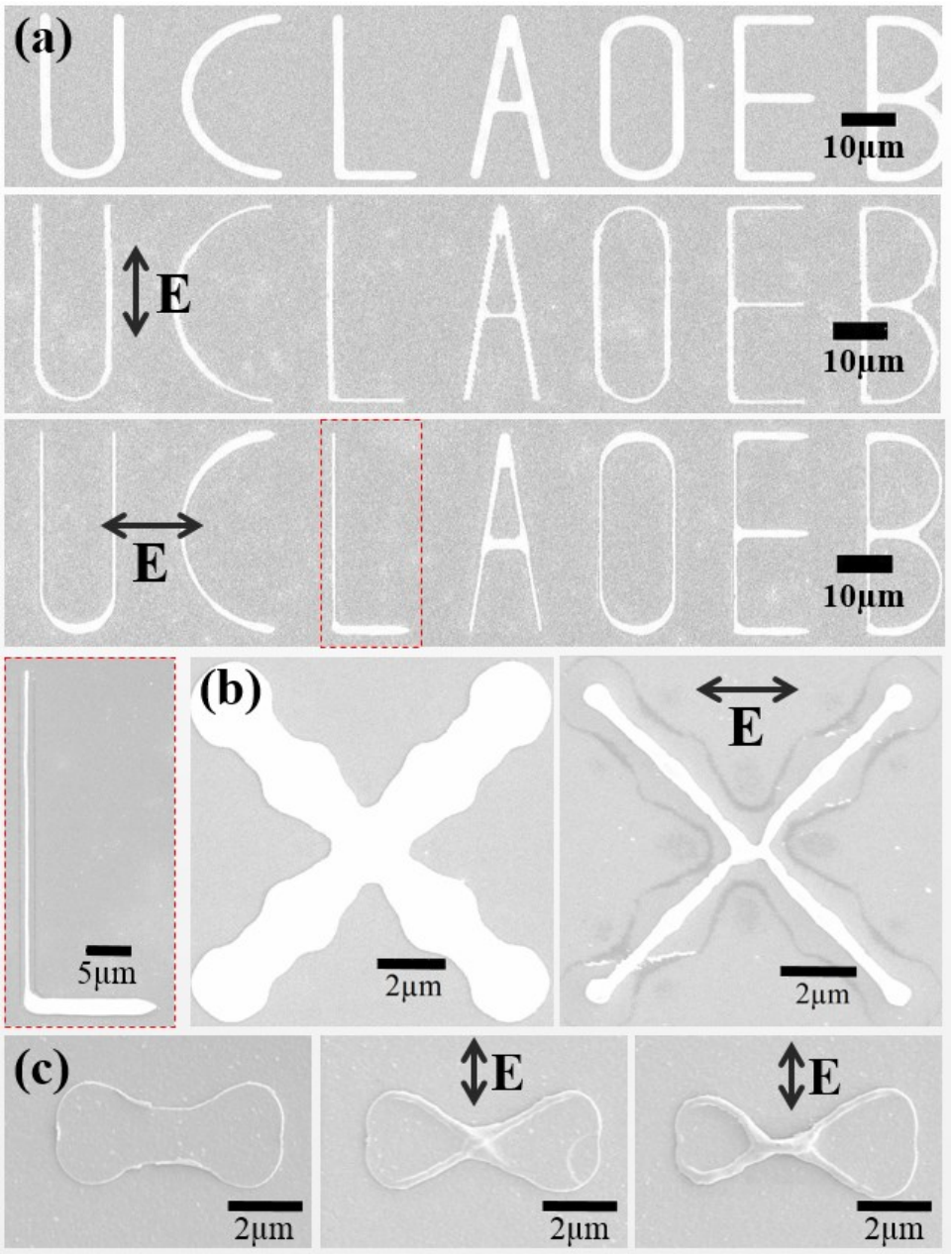

Figure 2.11 Reshaping of metallic structure depends on polarization of laser, pulse energy and pulse number.

Similarly, the shape of isolated 2D squares fabricated with periodic PDMS phase-shifting mold described in Section 2.2 can also be further shaped by flood exposure of few more laser pulses. If the periodicity of the mold is smaller than 2 μm, the laser cut 2D square usually has a dimension around 1 μm after melting and reflow. Although the electrical field is more enhanced in edges perpendicular to the light polarization and initiates heating in those area, due to large thermal diffusivity of gold, the heat quickly dissipates to other area and melts the whole micron-sized square. Therefore, instead of involving into rods, molten isolated metal squares ball up due to surface tension and form nanospheres with smooth surface. Fig. 2.12 shows the optical and SEM images of periodic gold nanosphere arrays using a 5/3 μm mold. The periodicity of the nanospheres in two dimensions can also be different by using grating with different periodicities. The size of nanospheres can also be tuned by mold periodicity and gold film thickness. A 6mJ laser pulse utilized in this experiment is able to print an area of 1 mm^2. Large printing area can be accomplished by scanning the light beams across the phase shift mask.

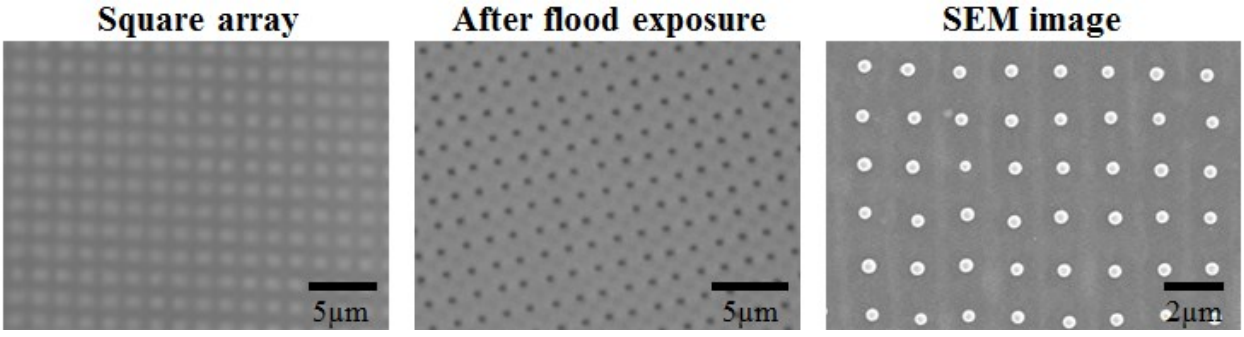

Figure 2.12 PDMS phase-shifting mold guided laser photothermally printed microsquares are transformed to nanospheres by flood exposure.

2.4 Printing on substrate with low thermal budget

Plastic and polymer are two common types of materials used as flexible substrates in electronic and photonic applications. The melting temperature of these materials is usually much lower than the melting temperature of metals and semiconductors. Pulse laser annealing is a commonly applied technology in electronic industry to obtain high quality polycrystalline film since it minimizes heating to the underlining substrates and is compatible with the low thermal budget of these low melting temperature substrates. In our near field photothermal printing technique, the pattern formation process takes place within 1 μs, so it permits direct metal printing on substrates that have low thermal budget. Shown in Fig. 2.13 is laser printing of a 100 nm thick gold thin film coated on a flexible PDMS substrate.

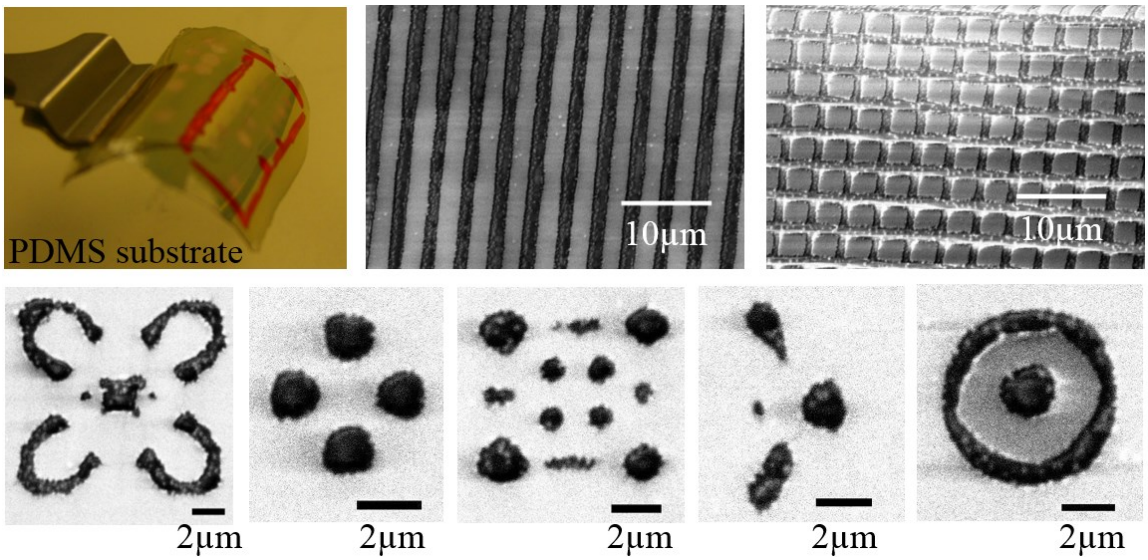

Figure 2.13 Laser printing of metallic structures on PDMS.

Chapter 3

Photothermal Transfer of Metallic Nanostructures

In previous chapter, there is noticeable imperfection in the ordering of nanosphere array, compared to microwire and microsquare array. During microwire and microsquare formation by PDMS phase shifting mold, there is always some area remaining cold and solid, anchoring on the substrate to maintain the periodicity of the array. However, in shape evolution of microsquare into nanosphere by flood exposure, whole area of microsquare becomes molten and balls up due to surface tension. The imperfection of ordering implies the possibility of molten gold jumping off the substrate, experiencing shape transition, landing on the substrate again and finally getting solidified. This phenomenon actually has been reported by A. Habenicht et al[18]. In their study, the flat gold nanostructure irradiated by a 10ns laser pulse became molten and contracted toward a sphere on a time scale of few nanoseconds. During this rapid shape change, the center of mass moved upward, leading to detachment of liquid droplets from substrate at an average velocity of 20m/s. Such imperfection in our photothermal reshaping experiment can be avoided or minimized if the microsquare array is spin-coated by photoresist before flood exposure.

Photoresist restrains the upward motion of liquid gold and helps keep it in position. However, in this chapter, we would like to take advantage of this "jumping" phenomenon to transfer gold nanostructreus to substrates on which direct fabrication of perfectly ordered nanoparticle array is difficult.

3.1 Introduction to laser induced transfer

Laser induced transfer (LIT) has been recently reported to transfer a variety of materials from one substrate to another. In a typical LIT setup, continuous flat film of interested material is deposited on inert substrates like graphite or glass. Illuminated by a tightly focused ultrafast laser pulse, nanofilm in the focal spot quickly gets melt, separates from surrounding solid film, and moves upward in form of a liquid nanodroplet. If there is another substrate right above the film in proximity distance, the jumping nanodroplet is received by the substrate and cools down on it as shown in Fig. 3.1. The substrate with flat film is called donor substrate, while the one receiving nanoparticle is named receiver substrate. Laser can illuminate through either donor substrate or receiver substrate, if they are not absorptive at laser wavelength. This technique is very versatile and has been reported to transfer all kinds of materials, including metal of different kind[19-22], silicon[23], oxides[24], and bio-materials[25]. Nanoparticles form different arrangement by precisely scanning independently positioned donor and receiver substrates[26]. Multiple layers of different materials can also be transferred with single laser pulse[27].

Femtosecond laser is most commonly used in laser induced transfer. First, the ultrafast pulse carries high light intensity to melt those low light absorbing or high melting temperature materials. Secondly, and more importantly if the material is metal, femtosecond laser provides

great spatial resolution due to a well confined heat-affected zone. Minimal heat is diffused into surrounding non-irradiated area due to the ultrashort pulse duration.

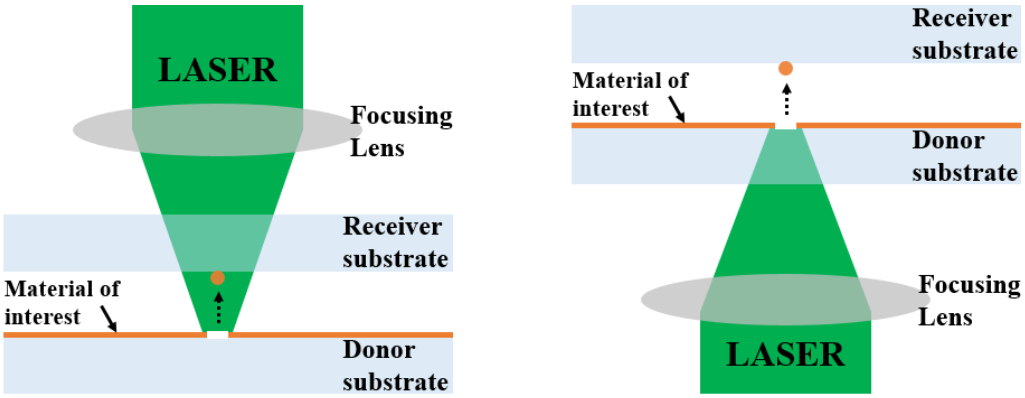

Figure 3.1 Schematic of laser induced transfer with laser illuminated from receiver substrate or donor substrate.

Laser energy fluence plays an important role in determining the size and morphology of the resulting deposited structure on receiver substrate[28, 29]. A general rule for most materials is that with laser energy fluence slightly above the melting threshold yet under transfer threshold, protrusion on continuous film will be formed, but no droplet is transferred. When the energy is increased above the transfer threshold to a moderate range of energy fluence, the transferred material keeps a sphere shape and the diameter increases with laser energy. Further increasing the energy will result in spread disk structure and finally multiple small droplets will spatter on the receive substrate due to explosion of overheated material.

The spacing between donor and receiver substrates is usually not critical. Spacing up to hundred microns has been used[22]. If no relative motion is required for donor and receiver substrates, they can be positioned in contact. In such contact, two rigid substrates are still

separated by a thin (~μm) air layer, due to dust particles trapped in between[30]. This is preferable for good quality of nanoparticle transfer with uniform size and precise localization.

To further improve the transfer throughput in case of application that requires large scale nanoparticle array, parallel transfer was proposed. Two types of strategies were used, given sufficient laser energy for both cases. First, a collimated laser beam can be split into thousands of laser hot spots by passing through a patterned photomask[31]. When illuminated on the continuous donor film, thousands of droplets can be transferred at the same time. Second, the continuous film is pre-patterned into numerous isolated micro or nano structures on the donor substrate[32 - 34]. Within an unfocused or defocused laser pulse irritated area, all islands will jump to the receiver substrate as shown in Fig. 3.2. In the latter approach, laser pulse duration is not critical any more for metal transfer, since the molten area of metal is self-limited by its pre-defined structure. Both femtosecond and nanosecond lasers can be used.

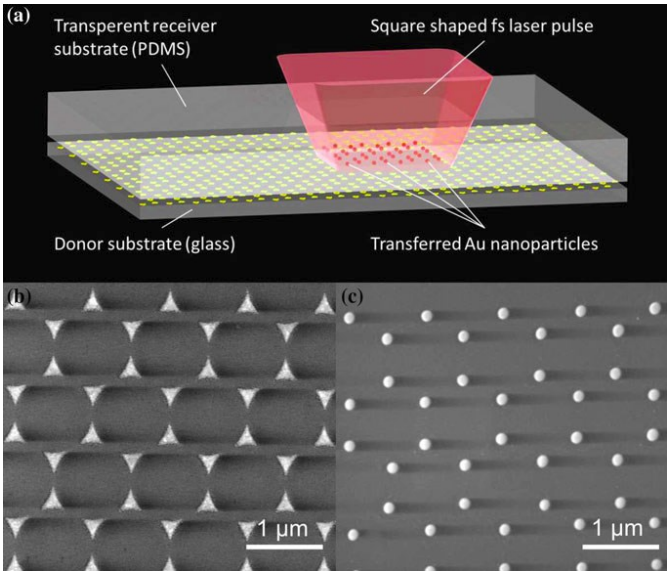

Figure 3.2 Schematic representation of laser induced transfer of pre-patterned donor substrate by nanosphere lithography for fabrication of nanoparticle array. Adapted from Ref. 34.

Our interest is to transfer large area gold nanoparticle array to PDMS substrate, flat and especially structured, since direct photothermal printing of gold nanoparticle array on PDMS is challenging due to poor interfacial properties between these two materials.

3.2 Large area transfer of gold nanoparticle to flat PDMS

We first test on large area laser induced transfer of good nanoparticle onto flat PDMS realized by collimated nanosecond laser pulse. On donor substrate, thin nanodisk array of good is patterned by either electron beam (E-beam) lithography or Stepper, which is a much more economical way, depending on the disk dimension we want. To our best knowledge, similar experiment has only been reported elsewhere using focused femtosecond laser beam 6μm x 6μm irradiated on nanosphere lithography patterned nanotriangle array on donor substrate[33]. They also showed SEM images of the transferred nanoparticle being partially (about 70%) embedded into the soft receiver substrate.

Optical setup

Fig. 3.3 illustrates the experimental setup. The laser source is a high power Nd:YAG laser (Surelite I, Continuum) with 6ns pulse duration and 532 nm wavelength. Laser energy arriving at the donor substrate is controlled by half wavelength plate and polarization dependent beam splitter. Although this high power laser is able to provide enough energy to cover its original beam size of 3 mm in diameter, we decide to use an iris diaphragm to select partial area of the beam due to the poor beam quality. The filtered beam has a Gaussian like energy distribution with 400μm full width at half maximum (FWHM). Sample is positioned on a

computer controllable motorized XY stage attached to a Zeiss Axio Scope microscope. Both bright field and dark field imaging mode are used to examine the transfer result.

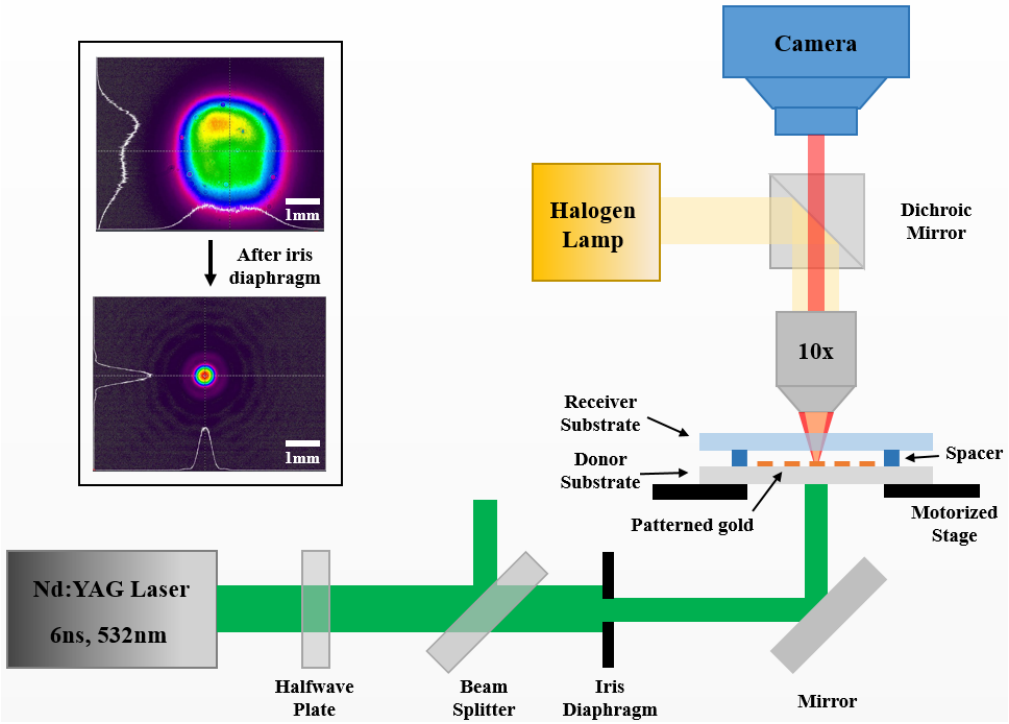

Figure 3.3 Schematic of the experiment setup for laser induced transfer of gold nanoparticle array.

Donor substrate preparation

Gold film is pre-patterned by means of E-beam lithography or Stepper on thin glass slide, followed by lift-off of later deposited metal. For nanodisk larger than 300 nm, Stepper is employed with advantage of high throughput and low cost. 10 nm gold is then deposited by e-beam evaporation. 1 nm Titanium is deposited between gold and glass substrate for most samples. After lift-off of undesired gold in acetone, spacer is patterned on the device. AZ-5214E is used as spacer, with a thickness around 1.6 μm.

Receiver substrate preparation

In order to get PDMS receiver substrate with flat surface, we pour uncured PDMS onto a pre-cleaned silicon wafer in a petri dish. For each experiment, a small piece of cured PDMS is cut out of the big PDMS slab, and quickly positioned with the clean surface (which is originally in contact with silicon) facing towards the donor substrate to avoid dust particle contamination.

Experiment and results

In our first run of this experiment, there is no spacer between donor and receiver substrates. Since PDMS is inherently soft, it collapses to donor substrate once they are brought into contact. It is different from "contact" situation reported by other groups where two rigid substrates are used. When two rigid substrates are in contact without external pressure, there is always an air gap due to dust particle or imperfect flatness of the substrate which prevents conformal and true contact. The pre-patterned nanodisk (300 nm in diameter, 10 nm in thickness) array appears red when observed in dark field mold. Upon laser exposure, nanoparticle within the laser irradiated area becomes golden and much brighter due to shape change, a sign of sphere formation. However, when PDMS is separated from donor substrate, no gold nanoparticle is found transferred to PDMS side. All nanoparticles stay on the donor substrate. This is possibly due to the kinetic energy of such a small volume being not big enough for gold nanodroplet to depart glass substrate and penetrate into PDMS, given that PDMS substrate tightly covered on top inhibits the gold nanodroplet to pick up speed and a thin titanium layer between gold and glass enhances the adhesion energy.

In order to confirm that transfer of our pre-patterned gold nanodisk cannot take place in a true contact mold, we cover the donor substrate conformally by photoresist, which is easier for

the gold nanodroplets to penetrate into than PDMS if transfer does happen. Fig. 3.4 shows positive photoresist AZ-5214E spin-coated on donor substrate. The thickness is around 1.6 μm. After laser irritation, photoresist is dissolved in acetone. If gold nanoparticles are transferred into photoresist, they should be gone with photoresist in this step. However, we find 98% percent of gold nanoparticles stay on donor substrate as shown in Fig. 3.4(b). The arrangement of array follows the nanodisk array before laser treatment, which implies the shape change driven by surface tension of molten gold happens on site. In a true contact mode, the upward motion is not strong enough to detach itself from donor substrate. The transferred nanoparticles have a spherical shape under SEM examination.

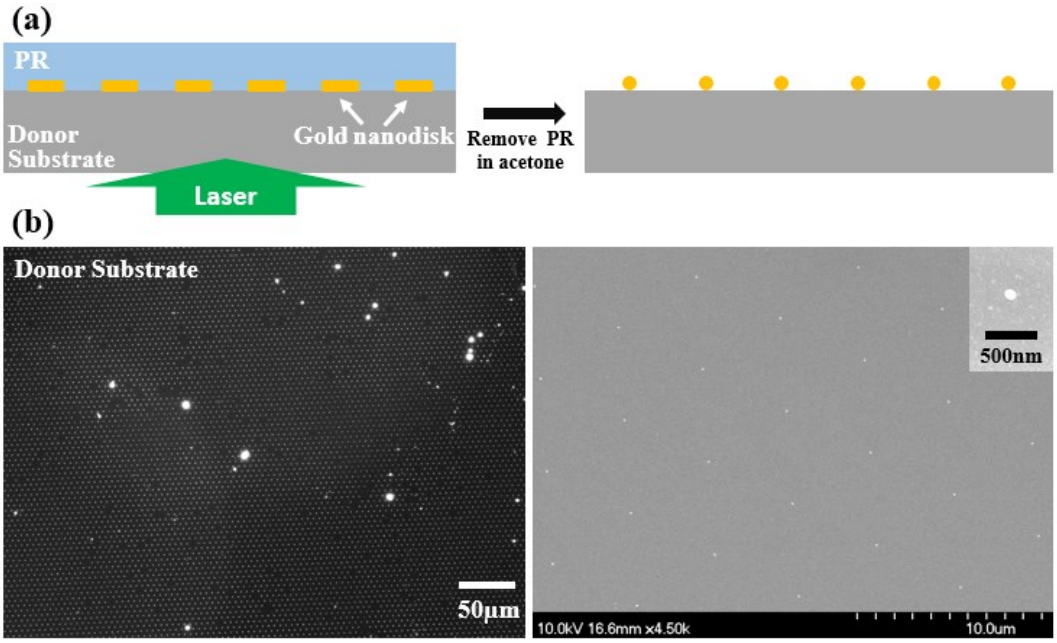

Figure 3.4 (a) Schematic of laser induced transfer when donor substrate is covered by unbaked photoresist; (b) When photoresist is removed in acetone, gold nanoparticles are found to remain on donor substrate, instead of transferring into photoresist.

Therefore, in all following experiments, we have spacer patterned within and around gold nanodisk area on donor substrate as shown in Fig. 3.5. The spacer is 1.6 μm thick positive photoresist AZ-5214E. When the soft PDMS receiver substrate is positioned on top of donor substrate, there is usually an air gap preventing the photoresist spacer to be in good contact with glass substrate. In this case, the spacer area is bright when observed under microscope as shown in Fig. 3.5(a). Area with gold nanodisk disk is left to the red dashed line. A gentle pressure is thus applied to force receiver substrate approaching spacer on donor substrate. When in contact, the spacer turns darker as shown in Fig. 3.5(b), and receiver and donor substrates are positioned ~ 1.6 μm apart. Within pre-patterned gold nanodisk area, the spacers are 125 μm apart. If the pressure is too large, soft PDMS will eventually collapse to the donor substrate. In Fig. 3.5(c), the gold area shows same color as spacer area, which implies that PDMS substrate is in true contact with glass substrate. In our experiments, first two situations allow gold nanoparticles to be transferred to PDMS side, while the last one does not.

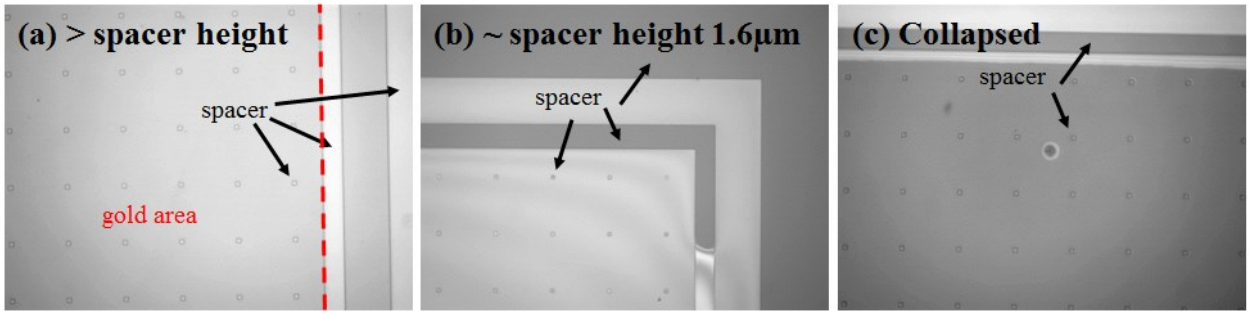

Figure 3.5 Spacing between donor and receiver substrates. (a) Spacing is larger than spacer height with no pressure applied; (b) Spacing is about spacer height with pressure applied to bring spacer and receiver substrate in contact; (c) PDMS receiver substrate collapses to donor substrate with too large pressure.

Laser energy is tuned to optimize the transfer result. Energy is measured before the iris diaphragm. An average of 6.5% energy is transmitted through the iris when it is rotated to have the smallest aperture. Fig. 3.6(a) shows the melting of pre-patterned gold nanodisk on donor substrate at different laser energy. For laser energy below 0.6mJ, no melting of gold nanodisk is observed. Above 0.6 mJ, melting area of gold nanodisk increases with higher incident laser energy. There is up to 10% energy fluctuation between pulses at the same setting, which is the reason that molten areas at 0.8 mJ and 0.9 mJ look similar. Energy between 0.8 - 1.0 mJ is empirically found to be a good energy window for reliable transfer. Example is shown in Fig. 3.6(b). On donor substrate, gold nanodisk in area not covered by the laser pulse still shows red color. Within the laser spot, the nanoparticles are missing due to being transferred onto receiver substrate. Nanoparticles on PDMS maintain the periodicity of nanodisk array, demonstrating one-to-one transfer from donor to receiver substrate.

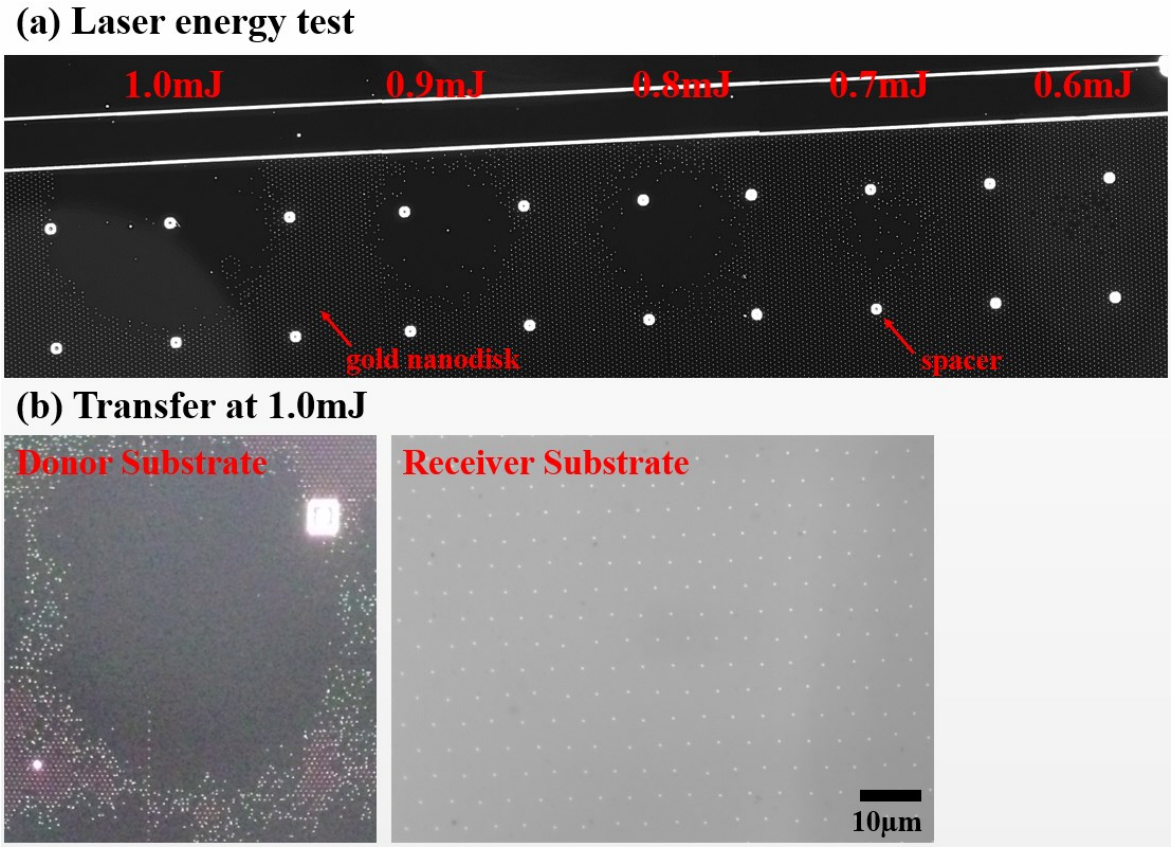

Figure 3.6 (a) Pre-patterned gold nanodisk array on donor substrate is pulsed at different laser energy. 0.8 ~ 1.0 mJ is found to be a good window for transfer. (b) Transfer result at 1.0 mJ. Un-irradiated gold nanodisk on donor substrate shows red color, and irradiated ones are gone on donor substrate. Nanoparticles transformed from those missed nanodisks are found on receiver substrate.

Fig. 3.7(a) shows transfer result when energy is further tuned over 1.0 mJ. When the energy is increased to 1.2 mJ, the center of the laser covered spot where the local energy fluence is highest is found to have no or few particles transferred to PDMS side. The reason is yet to be investigated. In areas away from the center, nanoparticles are still transferred due to irradiation by preferable lower energy fluence. The fluctuation of laser energy (averaged at 1.2 mJ) helps to reveal the trend of transfer result, which is higher energy of the laser is applied, more lost

nanoparticles are seen, starting from the center of laser spot and gradually spreading over the whole spot. However, when the laser energy is even higher at 2.0 mJ, nanoparticle array appears again on receiver substrate. This nanoparticle array scatters more green color, implying a smaller size compared to nanoparticles transferred at 1.0 mJ, which emits gold color. At such high energy irradiation, the nanodisk array on donor substrate is believed to evaporate and condense on receiver substrate[35]. Transferred nanoparticles at 1.0 mJ and 2.0 mJ are further compared side to side in optical and SEM images in Fig. 3.7(b) and (c). Corresponding images are taken at same configuration, same objective lens and same exposure time of camera for optical images, same magnification and voltage for SEM images. Significant size difference is noticed. Transferred nanoparticle at high energy is believed to lose some volume during evaporation and condensation.

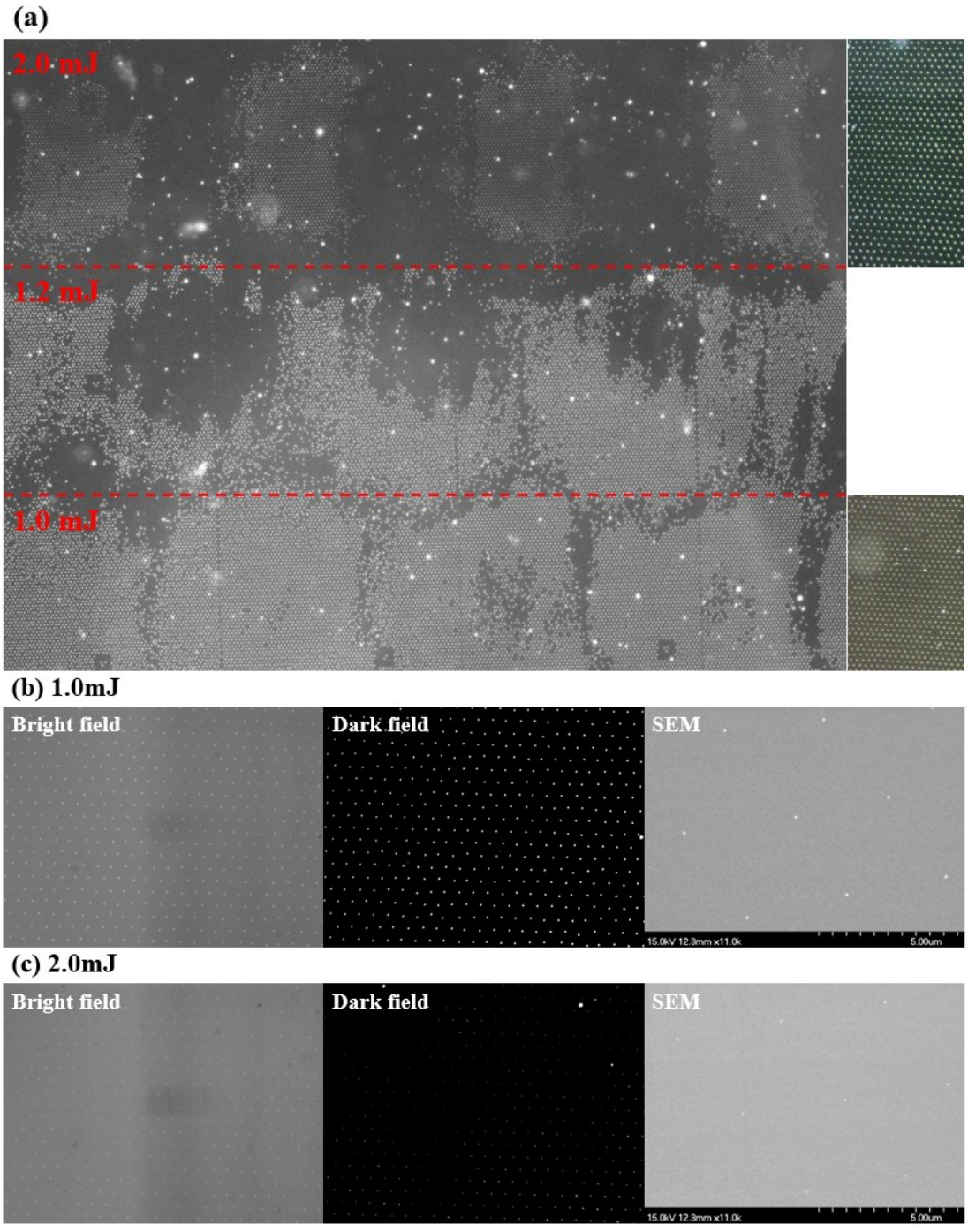

Figure 3.7 (a) Comparison of transfer result on PDMS at energy 1.0, 1.2 and 2.0 mJ. Transferred nanoparticle looks golden at 1.0mJ and green at 2.0mJ; (b) Direct comparison of transferred nanoparticles at optimal vs overdose energy of laser pulse by bright/dark field images and SEM images.

Time resolved image of cavitation bubble induced by transferred gold nanoparticle

In grazing incidence SEM image[33], gold nanoparticles transferred by femtosecond laser were seen partially embedded in soft PDMS receiver substrate, which provides stability and resistivity against cleaning and mechanical treatment of the sample. In order to check if the transferred nanoparticle by our nanosecond laser has similar result, instead of taking SEM image, we employed another approach which implies application values.

When a metallic nanostructure is immersed in aqueous media and heated with a short laser pulse, the temperature rises rapidly in the nanostructure and surrounding thin liquid layer. Upon surpassing an energy threshold that superheats the liquid medium, explosive cavitation bubbles can be induced, generating localized and high speed fluid flows[36]. With controlled nanoparticle density and triggering laser energy, gold nanospheres have been demonstrated to be useful in delivering biomolecules into live cell by opening transient membrane pores with small cavitation bubbles[10] or directly killing cancer cells by rupturing cell membrane with large cavitation bubbles[37].

Due to explosive expansion of cavitation bubble, the gold nanoparticle is usually propelled away if not mechanically anchored to a substrate. In laser induce transfer experiment, if transferred nanoparticles are partially embedded in PDMS, they are expected to stay in position, resistant to mechanical propelling force of rapid expanding cavitation bubbles. Fig. 3.8 shows time resolved images of cavitation bubbles induced by transferred gold nanoparticles. PDMS receiver substrate is immersed in deionized water. Same nanosecond laser is used to trigger the bubbles. Bubble images are taken at a 60ns delay after the onset of laser pulse, realized by synchronizing illumination source flash lamp with laser. As a reference, we take a time resolved image of the substrate but with no laser pulse applied. In such a situation, no

cavitation bubble is seen. Ten laser pulses are then irradiated on the same area with time resolved image taken for each pulse. In all images, cavitation bubbles are seen to have an arrangement coinciding with that of transferred nanoparticle array and the arrangement doesn't change over ten pulses. This proves that the transferred nanoparticle is embedded in PDMS substrate to some extent, anchoring itself against propulsion from cavitation bubble. The size of cavitation bubble in 10^{th} laser pulse looks smaller than that in 1^{st} pulse. This is probably caused by partial volume of gold nanoparticle being evaporated by laser pulse with too high energy.

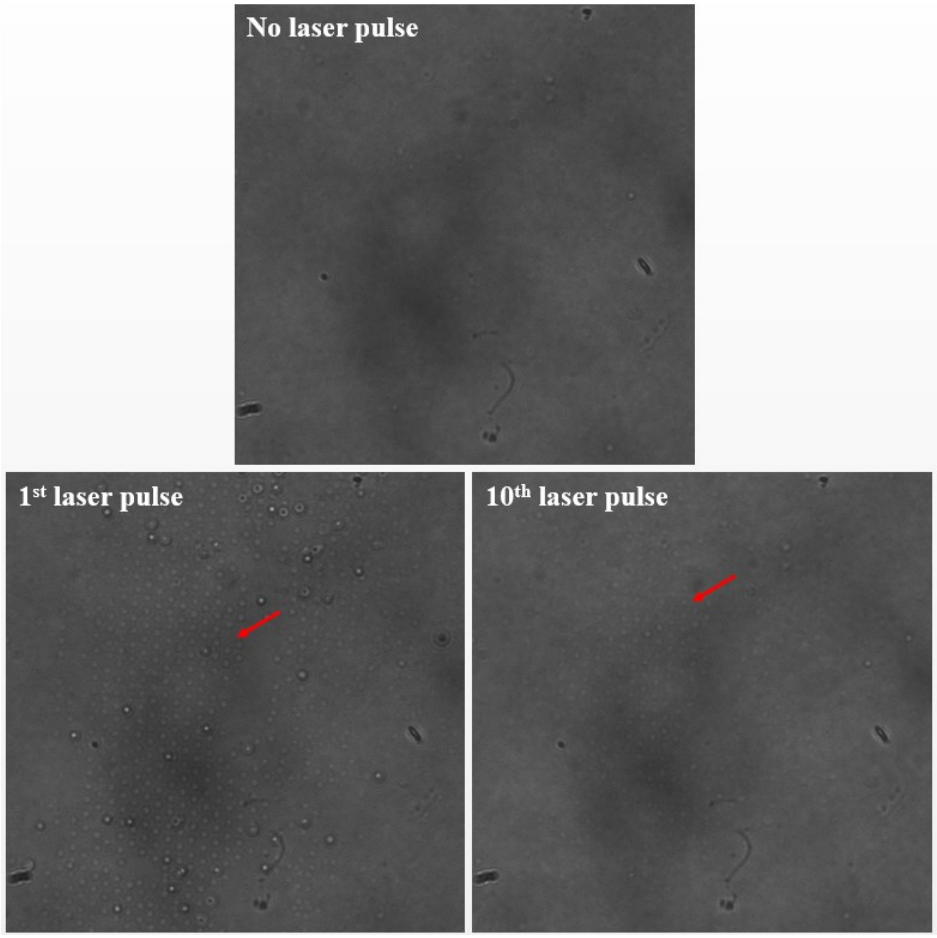

Figure 3.8 Time resolved images of cavitation bubbles induced by laser heated gold nanoparticle array that is transferred into PDMS substrate.

3.3 Large area transfer of gold nanoparticle to PDMS pillar array

We further conduct a study on laser induced transfer of gold nanoparticle to structured PDMS receiver substrate, to be more specific, PDMS micropillar array. PDMS micropillar array has been intensively used as cell force sensor to monitor interaction between cell behavior and external environment, especially mechanical stimuli, to understand a variety of biological events[38, 39]. Top of the pillars are fluorescently labeled to obtain a high contrast between the tip of the pillars and background. Intensity profiles of the fluorescent pillar tips are modeled by a two-dimensional Gaussian fitting to get the pillar position and therefore the deflection with cells growing on top. Local traction force is then calculated by multiplying the deflection of pillar tip by the pillar stiffness. Objective lens with high magnification (larger than 60x)[40, 41] are usually used to get good precision 30~50 nm of pillar position. However, for object larger than the diffraction limit of an optical system used, it's not appropriate to use Gaussian fitting since the profile of pixel intensities are not described by a Gaussian[42]. Besides, such highly magnified optical system limits the area that one image can cover and makes it incapable of monitoring large scale concurrent and instantaneous collective cell behavior. In order to address these challenges and maintain high precision at the same time, we propose to use gold nanoparticle embedded micropillar array. Gold nanoparticle provides point-source like strong plasmonic scattering signal when imaged by objective lens of low magnification (20x or less). Intensity profile of a point-like source, especially with high signal-to-noise ratio, can be perfectly fitted by Gaussian function with sub-pixel resolution.

Fabrication of metal pattern on flat PDMS is usually realized by three methods: (1) Direct patterning on PDMS by either wet etching or lift-off[43-45]; (2) deposition of metal on PDMS

through a patterned shadow mask[46]; (3) transfer of pre-patterned metal on a solid substrate to PDMS[47, 48]. Among them, the last approach provides best reliability and durability of metal since the metal is embedded in the surface of PDMS (Fig. 3.9(a)). Gold nanoparticle array can also be embedded in a planar PDMS substrate by this pattern transfer method[49] as shown in Fig. 3.9 (b).

To fabricate metal nanostructure on a structured PDMS substrate is more challenging. Fabrication of arrayed gold nanoparticles in PDMS holes has been reported by removing metal film on top surface of PDMS substrate followed by laser pulsing gold micro/nano disks left at the bottom of hole[50] as shown in Fig. 3.9(c). One nanoparticle sits in one hole.

To date, fabrication of nanoparticle array sitting on the tip of arrayed PDMS micropillar with 1:1 mapping has never been reported. Here we propose to fabricate gold nanoparticle embedded PDMS micropillar array by laser induced transfer.

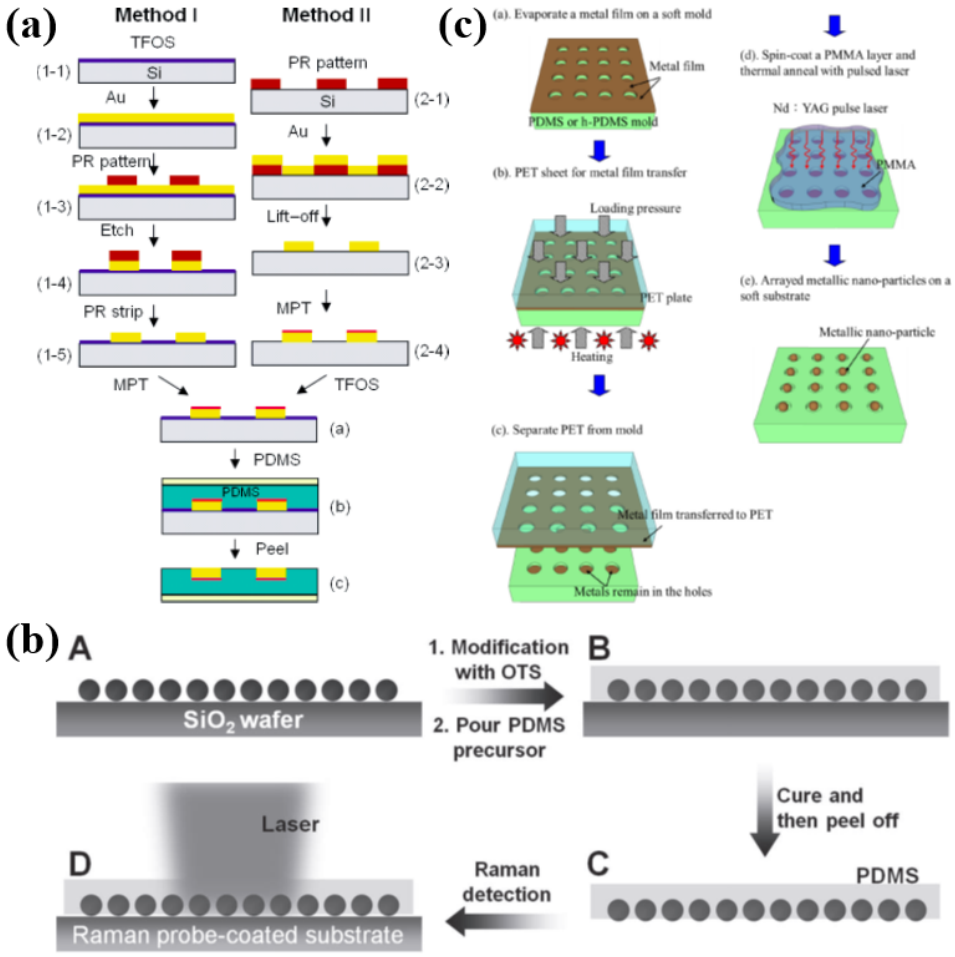

Figure 3.9 (a) Metallization of PDMS by pattern transfer; (b) Fabrication of gold nanoparticle array embedded PDMS; (c) Laser assisted formation of gold nanoparticle in PDMS hole array. Adapted from Ref. 48-50.

We first come up with an idea of transfer pre-patterned gold nanodisk on glass substrate to pre-made PDMS pillar array as illustrated in Fig. 3.10(a). Gold nanodisk donor substrate is prepared in the same way as samples used in Chapter 3.2. Gold nanodisk and PDMS pillar are precisely aligned and brought towards each other till the spacing between two substrates is reduced to the spacer height. Laser pulses are irradiated on pillar area as well as surrounding flat PDMS area. Fig. 3.10(b) shows the result after PDMS is separated from glass substrate. Most

gold nanodisks under flat PDMS area are transferred to PDMS side, while only a small portion of gold nanoparticles are transferred to pillar side (top, sidewall as well as base of pillar) as indicated by white arrows. We examine the donor substrate and find that most nanoparticles transformed from nanodisk remain on this substrate. This direct comparison between transferring to PDMS pillar and to flat PDMS implies that topography of the receiver substrate has an impact on transfer result. Although how the impact takes place is unclear, we have a suspicion that the unflat top of PDMS pillar strongly backscatters the laser light that obstructs the jumping nanoparticles to reach the receiver substrate.

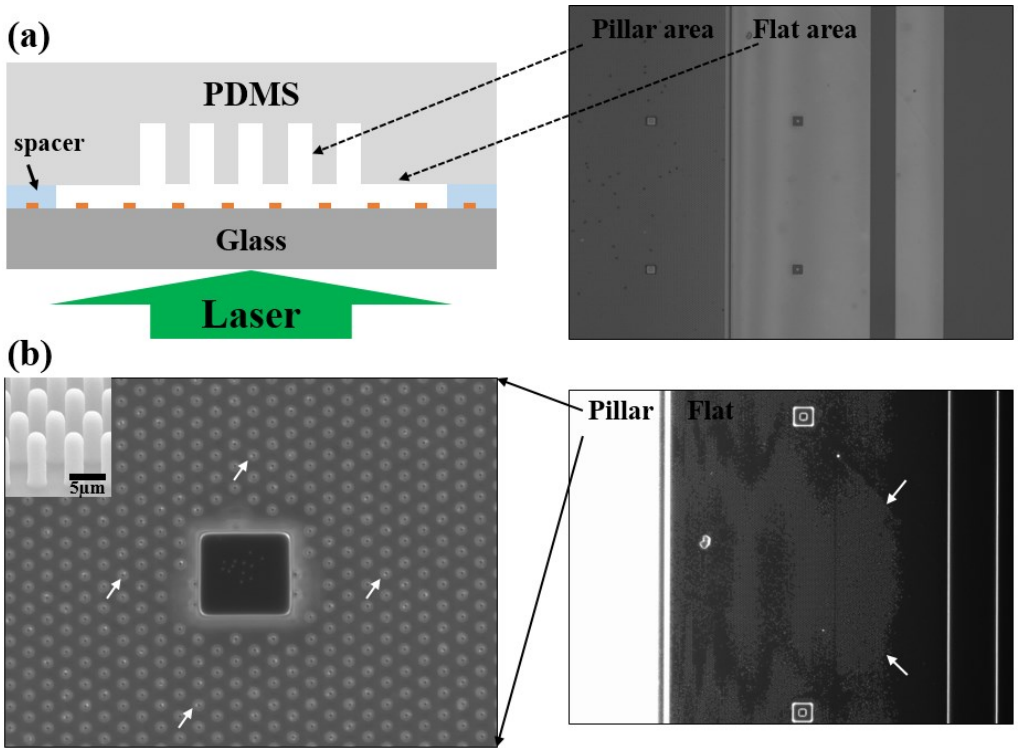

Figure 3.10 Attempt of transferring pre-patterned gold nanodisk on glass substrate to pre-made PDMS pillar array.

Fig. 3.11 illustrates the final process flow of fabrication of gold nanoparticle embedded PDMS micropillar array. Silicon wafers are piranha-cleaned and sent into oxidation furnace

configured for wet oxidation at 1150°C. An average of 500nm thick silicon oxide is grown after 30 minutes. Positive photoresist AZ-5214E is spin-coated on the wafer and patterned by conventional photolithography. The pattern is transferred to SiO_2 layer by etching the oxide in AOE (advanced oxide etch). Photoresist is stripped in acetone afterwards. SiO_2 is then used as etching mask for silicon pillar array etching in DRIE (deep ion reactive etching). Silicon pillars with vertical and smooth sidewall can be fabricated with a recipe listed in Table 3.1. The selectivity between SiO_2 and Si by this recipe is about 1: 25, with an average etching rate of 4nm/loop and 100nm/loop respectively. Once desired height of pillar is achieved, SiO_2 on both sides of wafer is removed in hydrofluoric acid. This silicon pillar array is the master mold for a following two-step replication process to fabricate PDMS pillar, so silicon pillar of different heights are obtained to allow optimization of the final PDMS pillar stiffness.

Silicon master mold is treated with 10 µl silane in a vacuum chamber overnight. PDMS precursor (degased mixture of Sylgard 184 elastomer and curing agent, w/w = 10:1) is poured on silicon and cured at 80°C for over 24 hours. If the time is not long enough, we sometimes find uncured PDMS at edge of silicon mold. After complete curing, the PDMS negative mold can be easily peeled off from the silicon master and tailored using a razor blade. The PDMS negative mold is positioned in a petri dish alongside a glass slide with 7 µl silane dispensed on it. The petri dish is degased in a vacuum chamber for 1 hour and then left in vacuum for 18 hours. 20/1/40 nm thick SiO_2/Ti/Au multilayers are deposited on the PDMS mold in an e-beam evaporation system (CHA Mark 40, CHA Industries, Inc.) with a deposition rate of 1/0.2/1 Å/s. Gold on top surface of PDMS mold is peeled away by adhesive tape after one day of deposition, leaving only gold microdisk at the bottom of PDMS well. A similar step of silane surface treatment is carried out again to facilitate the final demolding of PDMS pillar from PDMS

negative mold. 3 µl silane is used instead. After treatment, small amount of degased uncured PDMS is dropped on PDMS mold and vacuumed in a reactive ion etch machine (Technics Micro-RIE Series 800, Technics Inc.) down to 20~30 mtorr for the microwells to be fully filled. An oxygen plasma treated thin glass slide is usually covered on top of uncured PDMS as a rigid substrate for PDMS pillar array after demolding. After PDMS is cured at 80°C for 24 hours, nanosecond laser pulses are applied to transform gold microdisks sandwiched between PDMS mold and PDMS pillar into nanoparticles, which meanwhile detach from bottom of PDMS well and penetrate into PDMS pillar tip during the rapid shape evolution. Gold nanoparticle embedded PDMS pillar array is slowly demolded from PDMS mold and examined under optical microscope and SEM.

Table 3.1 Bosch recipe for etching silicon by DRIE.

Step	Pressure (mTorr)	Gas Flow (sccm)			Power (W)		Set Time (sec)
		C_4F_8	SF_6	Ar	RIE	ICP	
Passivation	18	30	0.5	12	0.5	825	5
Etch A	18	0.5	15	12	8	825	2.5
Etch B	18	0.5	30	12	10	825	4

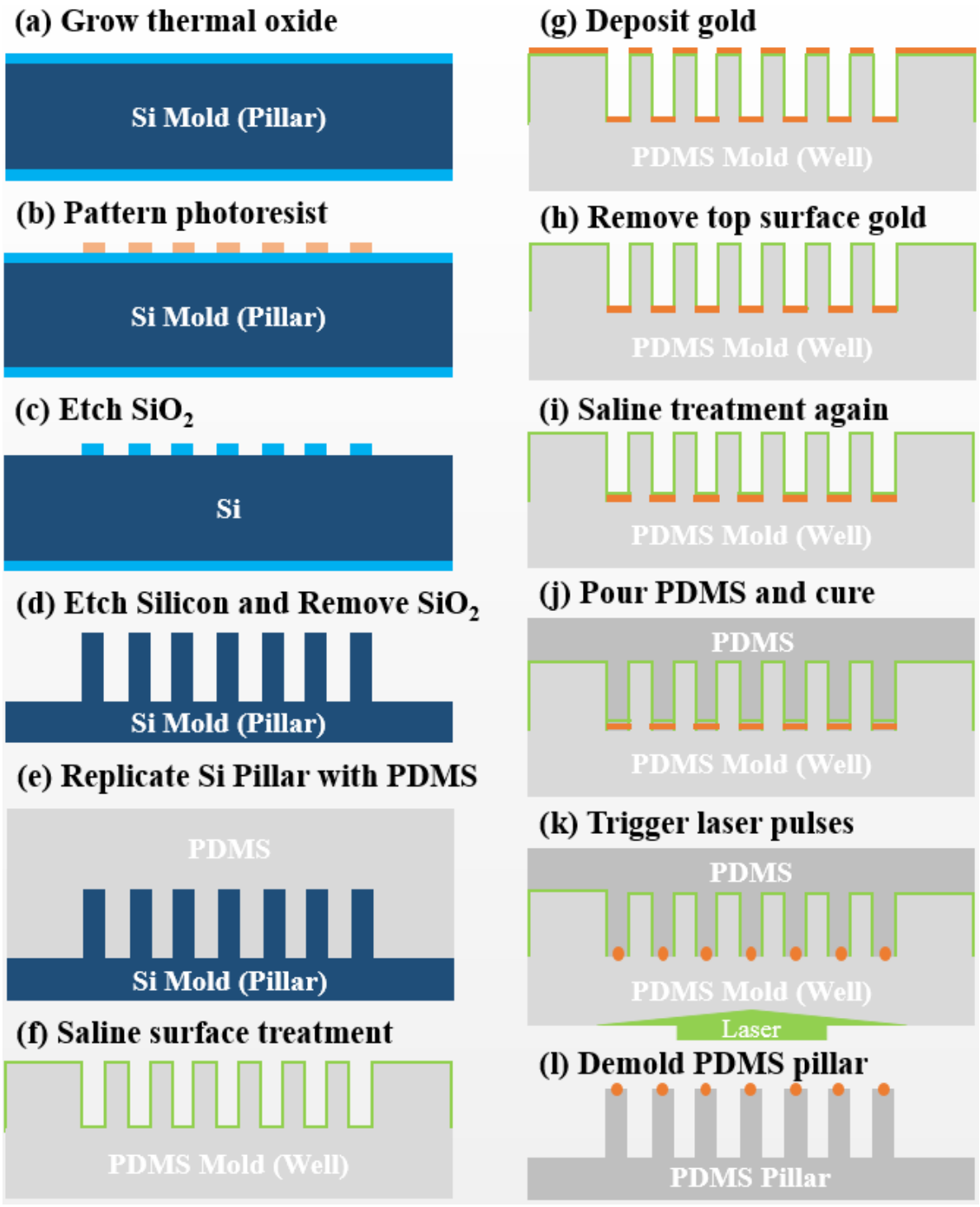

Figure 3.11 Schematic process of fabrication of gold nanoparticle embedded PDMS micropillar array.

Several steps during the fabrication process need to be pointed out to ensure the reliability and repeatability of this process. First, the time between metal deposition by CHA and top surface metal removal by yellow tape has to be at least one day in all our experiments. Otherwise, insufficient lag time will result in a lot of residual gold patches left on PDMS mold as shown in Fig. 12(a). The gold residuals can also be transferred to base of PDMS pillar by laser pulses along with nanoparticles of interest transferred to the tip of pillar. In dark field imaging mold, these big gold particles at base will strongly scatter light, acting as undesired background noise for nanoparticle sitting in tip of pillar. Second, thin SiO_2 layer between gold and PDMS is necessary. PDMS has a very low surface energy[51], which not only makes metal hard to adhere, but also makes the spontaneous dewetting of metal easier. If there is no SiO_2 underneath the gold microdisk, the microdisk will dewet into multiple tinier particles during molten state instead of evolving into single one as shown in Fig. 12(b). Third, amount of silane surface treatment in Fig. 3.11(i) should be sufficient. The threshold is pillar height dependent. At the level when short pillars can be easily demolded, taller pillars may break at base and stay in PDMS well as shown in Fig. 12(c). However, overdose of surface treatment also should be avoided. Silane is deposited on PDMS surface in a layer-by-layer fashion timed by the hours PDMS stays in the vacuum chamber full of silane vapors. Too many layers will reduce the apparent diameter of PDMS well and even fully fill the microwell eventually. Forth, during the final demolding process, pillars may collapse due to high aspect ratio. Collapsed pillars are sonicated in methanol to make the micropillars stand upright and then supercritically dried in a critical point drier.

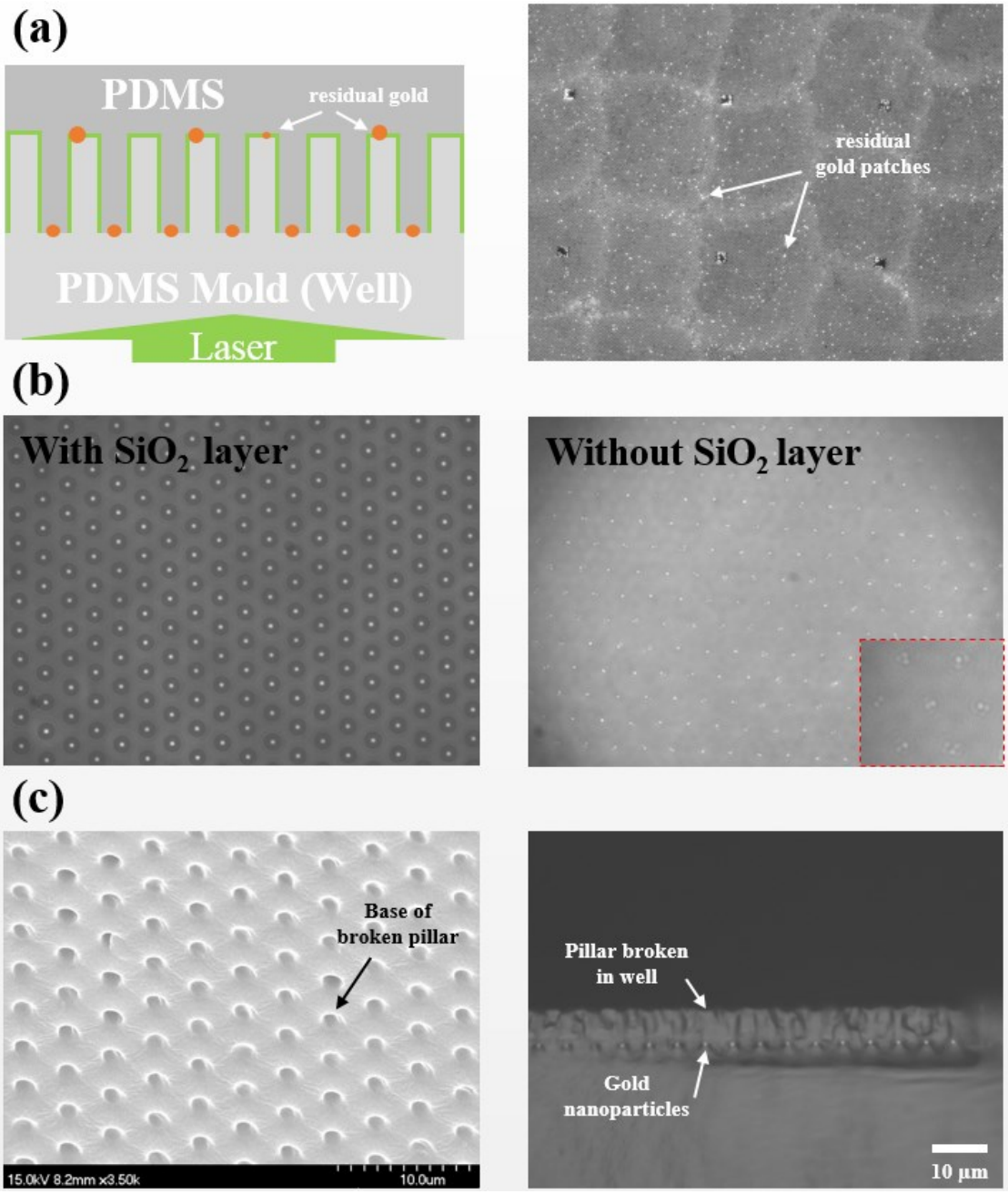

Figure 3.12 (a) Residual gold patches left on PDMS mold will be transferred to pillar base; (b) Gold microdisk dewets into one nanoparticle with SiO_2 underneath, but into multiple tinier ones without SiO_2; (c) Pillar breaks at base and stays in microwell when silane surface treatment is not sufficient.

Laser induced transfer is the most important step in whole fabrication process. Gold microdisks sandwiched between PDMS pillar and its mold are melted and evolve, driven by surface tension of molten gold, into nanoparticles as shown in Fig. 3.13(a). This can be achieved by single laser pulse. Insufficient laser energy will result in rod-shaped gold structure, probably due to insufficient melting time for the material to complete the migration towards the center. When PDMS micropillars are demolded from the PDMS mold, nanoparticles within the laser-irradiated area are transferred into micropillars. This is confirmed by SEM images Fig. 3.13(b). In tilted SEM images, the gold nanoparticles seem to be embedded in PDMS. In order to get a clear view of this, half of the pillar is removed by focused ion beam (FIB) as shown in Fig. 3.13(C). The cross section images show that gold nanoparticles are actually partially embedded in the tip of the pillars.

Ideally, laser beam can be expanded as large as energy permits to transfer large area of gold nanoparticles in one pulse. In our experiment, the Gaussian like laser beam used in Chapter 3.2 is expanded twice by a concave lens (f = -75 mm, LC4513, Thorlabs). Thus the laser arriving at PDMS sample has a beam width of 800 μm at FWHM. Laser energy within an energy window ($E_{min} \sim E_{max}$) can be used. If energy is larger than E_{max}, gold in the center of the pulse will evaporate and transferred nanoparticles will be visibly smaller than surrounding area. If energy is smaller than E_{min}, gold microdisk cannot fully evolve into a spherical nanoparticle. Optimal energy will be slightly under E_{max} to transfer gold nanoparticles with similar dimension in an area as large as possible. 1 mJ is finally selected to cover an area of around 450 μm in diameter. The average energy fluence irradiated at gold microdisk is around 400 mJ/cm^2. At this experiment condition, 97.5% of gold nanoparticles within the field-of-view (FOV) of a 20× objective lens (EC Epiplan-Neofluar 20x/0.5 HD, Zeiss) imaged by our CCD camera (AxioCam

MRm, Zeiss), 450 µm x 340 µm, are successfully transferred to pillar tips as shown in Fig. 3.14. The 2.5% loss of gold nanoparticles could be attributed to three parts: demolding process, insufficient energy in the area away from laser spot center, and overtime sonication. The latter two can be solved by using laser pulse with flat-top beam shape and shorter sonication time.

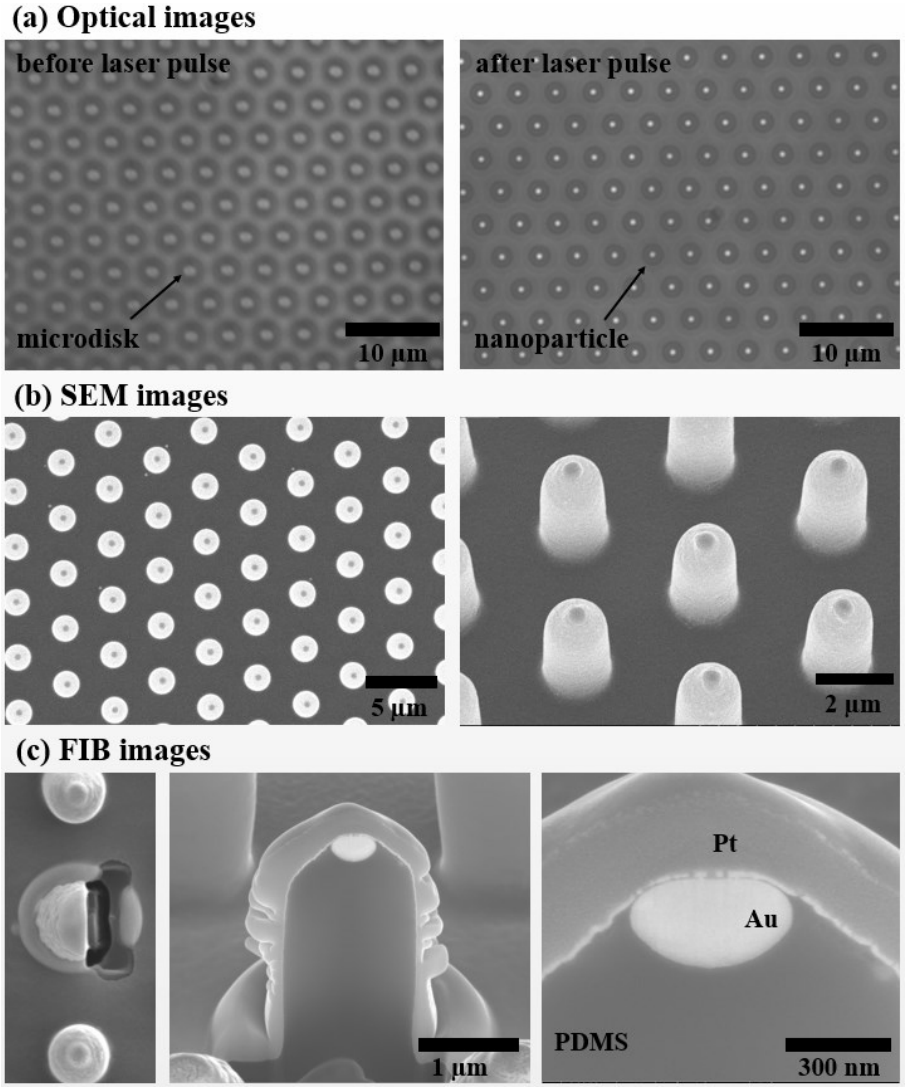

Figure 3.13 (a) Gold microdisks sandwiched between PDMS pillars and its mold are melted by laser pulses to form nanoparticle and; (b) SEM images confirm gold nanoparticles are transferred to pillar top; (c) FIB images show that each pillar has one gold nanoparticle anchored in the pillar top.

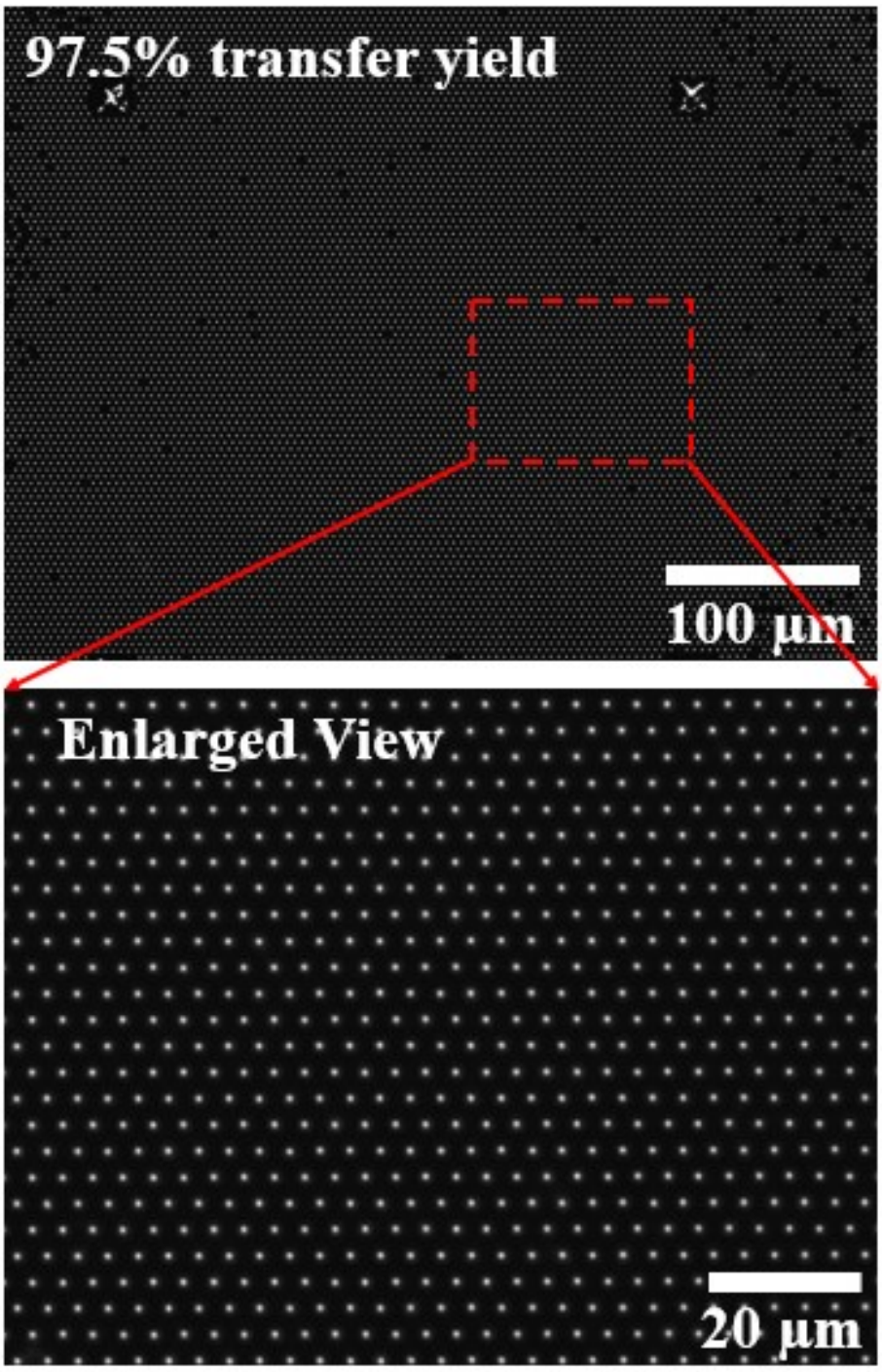

Figure 3.14 97.5% of nanoparticles within the FOV of a 20× objective lens are successfully transferred.

Chapter 4

Large Area Sensitive Plasmonic Cell Force Sensor

4.1 Introduction to micropillar array cell force sensor

Microfabricated elastic pillar substrates of various geometries found widespread applications to address many fundamental questions in cell biology regarding the mechanotransduction of cell functions[52-59]. The tip of pillar is usually fluorescently labeled to obtain high contrast between the pillar and background in the image. Intensity profile of the fluorescent pillar tips is then modeled by a two-dimensional Gaussian fitting to get the pillar position and therefore deflection with cells growing on top. Local traction force is finally calculated by multiplying the deflection of pillar by pillar stiffness. Objective lenses with high magnification (larger than 60x)[58-60] are usually used to get a good precision 30~50 nm of pillar position. However, the coated fluorescent proteins can be degraded and/or digested by the cells, and dissolved in the media especially during the media swapping. Therefore the quality of fluorescent image is degraded in a time dependent manner, which will affect the accuracy of the

dynamic cell force measurement[61]. Besides, for object larger than the diffraction limit of an optical system used, it's not appropriate to use Gaussian fitting since the profile of pixel intensities is not described by a Gaussian[42]. Such highly magnified optical system also limits the area that one image can cover and makes it incapable of monitoring large scale concurrent and instantaneous collective cell behavior. In order to address these challenges and maintain high precision at the same time, we propose to use gold nanoparticle embedded micropillar array. Gold nanoparticles provide point-source like strong plasmonic scattering signal when imaged by objective lens of low magnification (20x or less). Intensity profile of a point-like source, especially with high signal-to-noise ratio, can be perfectly fitted by Gaussian for sub-pixel resolution.

4.2 Gold nanoparticles embedded PDMS micropillar array

Generally a source of light can be considered a point source if the resolution of the imaging instrument is unable to resolve its apparent size. The resolution of an optical system is usually assessed by Rayleigh criterion[62] which states as the first diffraction minimum of the image of one coincides with the maximum of another as shown in Fig. 4.1(a). This diffraction limited resolution r for a conventional optical microscope can be calculated as $r = 0.61\lambda/NA$ for a circular object, where λ is the wavelength of illumination light source, n is refractive index of the medium, and NA is numerical aperture of the objective lens used in the microscope. If the dimension of the object to be imaged is smaller than the resolution, this object cannot be resolved in the image. In our case, the diameter of gold nanoparticle embedded in the pillar tip is smaller than the diffraction limit when a 20x/0.5 objective lens is used in the microscope, thus

the nanoparticle which strongly scatters the illumination light in dark field imaging mold can be treated as a point source or point object for subsequent image analysis.

Intensity profile of a point source in an optical system can be described by the point spread function (PSF). The Airy PSF is valid and commonly used for most optical systems but tedious for many practical calculations, so PSF of a circular point source is often approximated by a Gaussian function. This is the foundation for us to model the image of the gold nanoparticle by a two-dimensional Gaussian function. The pillar position with sub-pixel precision is determined by the least-square fit to this model. The fitting precision strongly depends on the number of pixels selected to fit and the signal-to-noise ratio. The area in an image where pixels are selected for Gaussian fitting is usually called an estimation mask. If the mask is much broader than the image of the object of interest, a lot of background noise will be taken into account which may skew the centroid estimate[63]. Otherwise if the mask is too small compared to the image, lack of effective information will also deteriorate the fitting result. In our image analysis, an estimation mask that is tightly large enough to cover an area of twofold standard deviation on each side of the Gaussian PSF is selected for fitting as shown in Fig. 4.1(b). For the signal-to-noise ratio, normally higher it is, more accurate the fitting is. Thompson et al. derived a more specific equation to quantify the fitting accuracy $\Delta\chi$ as[64]

$$\Delta\chi = \sqrt{\frac{\sigma^2 + a^2/12}{N} + \frac{8\pi\sigma^4 b^2}{a^2 N^2}} \qquad (1)$$

Where σ is standard deviation of the Gaussian PSF, a is the physical size of the pixel, b is background noise, and N is the object signal to be fitted. With moderate or better signal-to-noise ratio, it's not difficult to obtain a precision better than 1/10 pixel[65].

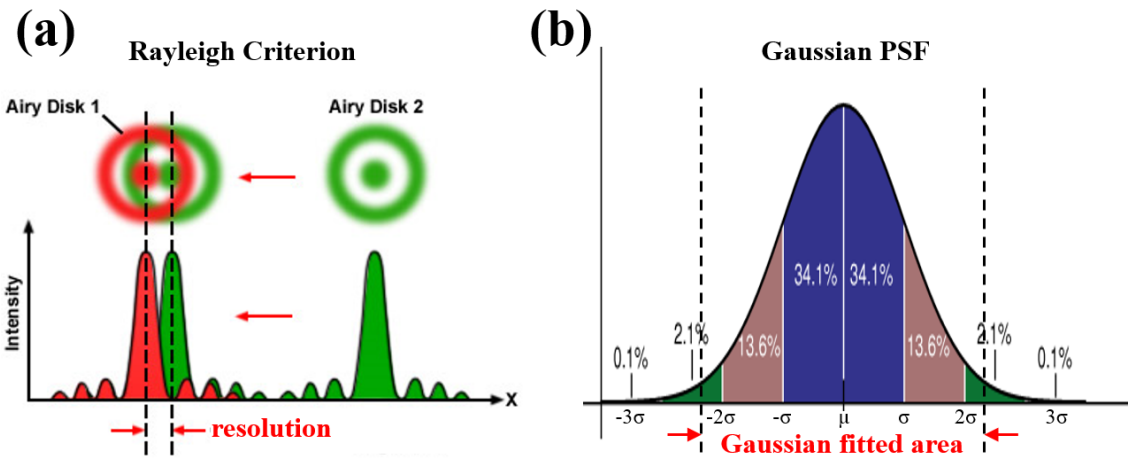

Figure 4.1 (a) Resolution of a diffraction limited optical system is assessed by Rayleigh criterion; (b) An area larger than twofold standard deviation is selected for Gaussian fitting.

In our experiment, the plasmonic micropillar array is immersed in cell culture media, Dulbecco's Modified Eagle Medium (DMEM, Life Technologies) supplemented with 10% FBS (Hyclone) and 1% penicillin and streptomycin, in a petri dish. The sample is positioned under an upright microscope (Axio Scope A1, Zeiss) equipped with a 20x, N.A. 0.5 objective lens (EC Epiplan-Neofluar 20x/0.5 HD, Zeiss). The CCD camera (AxioCam MRm, Zeiss) used to take the image has a chip area of 8.9 mm x 6.7 mm with pixel size of 6.45 μm x 6.45 μm. All images are taken in dark field imaging mode.

When PDMS pillar is immersed in cell culture media, the scattering from the pillar, a source for background noise in our analysis, is suppressed compared to that in air. This is due to a much smaller refractive index difference between PDMS and the media (mainly water), 1.4:1.33, as contrast to PDMS and air, 1.4:1. However, we find the media thickness above our device has an impact on the signal-to-noise ratio. 4 ml culture media is first added into the petri dish, resulting in about 1 mm thick media coverage above the PDMS device. Right after the

plasmonic scattering signal of certain area in the PDMS device is captured, 2 ml media is aspirated by a pipette. Image on the same area of the plasmonic pillar array is taken again. Exposure time for each image is adjusted so that the pixel of highest intensity, which always comes from the gold nanoparticle, is right under-saturated. Much brighter background around gold nanoparticles can be seen in the image when pillar is covered with a thicker media layer as shown in Fig. 4.2. Therefore in all following experiments, culture media is controlled to be 2 ml or less during image capture.

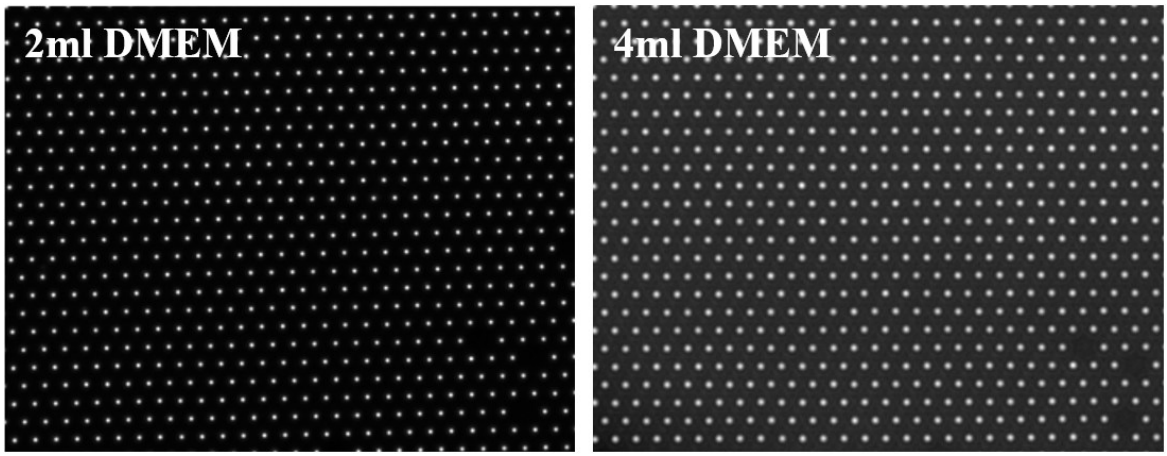

Figure 4.2 Signal-to-noise ratio is dependent on the media thickness above the plasmonic pillar.

Fig. 4.3 gives an example of the image of a gold nanoparticle fitted by a Gaussian function. The fitted center of the Gaussian function represents the pillar position. Effective pixel size in the image is 322.5 nm, calculated by pixel size in the CCD chip divided by the magnification of objective lens. The standard deviation of the imaging system is estimated by $\sigma \approx \frac{0.21\lambda}{\mathrm{NA}} \approx 230\ \mathrm{nm}$, where wavelength 550 nm is selected to represent the illumination from a halogen lamp. NA equals to 0.5. Number of pixels is selected by the criterion stated above when

the estimation mask fully covers an area of total four-fold standard deviation. In our analysis, we also take the real size of gold nanoparticle ~ 400 nm into account, so the number of pixel used for Gaussian fitting is 5 by 5 to cover an area of (400 + 230*4) nm in diameter. The average signal-to-noise ratio is 20 in the image, giving an average fitting accuracy $\Delta\chi$ of 40 nm according to equation (1). However, our case is not identical to the one described in the literature, thus a fitting accuracy on the same order of tens nanometer is acceptable in our analysis.

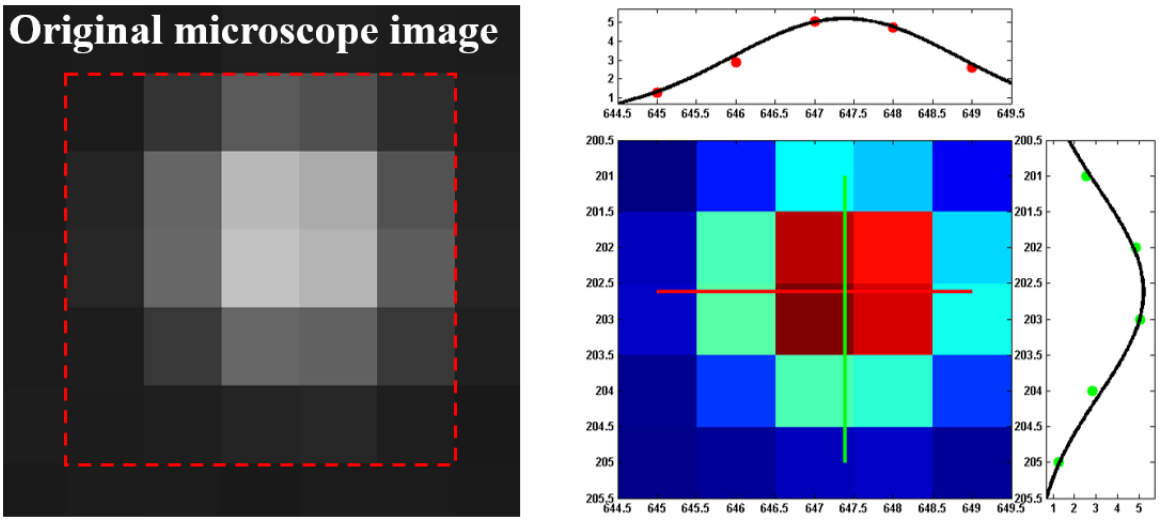

Figure 4.3 Gaussian fitting of a gold nanoparticle imaged by 20x objective lens.

4.3 Precision of pillar localization by plasmonic PDMS pillar array

The key point of our gold nanoparticle embedded PDMS micropillar in the application of cell force sensing is to enable precise force measurement when imaged by less magnified optical system in order to concurrently monitor a larger volume of cells. Pillar localization precision is usually a direct measure of the precision for cell force, since the cell force can be simply deduced by pillar deflection multiplied by pillar stiffness. Some of reported precisions are summarized in

Table 4.1. A CCD camera with 6.45 μm x 6.45 μm pixel size is used in most of the references. We can see there is huge precision difference in cases when 40x objective lens is used, so we don't take these data into account.

There are different criterions used when it comes to precision or resolution. Prof. Benoıˆt Ladoux's group proposed to use systematic error, which is estimated from the measured deflection of pillars in an area absent of cells[59, 66]. In the analysis, they selected partial area of the image where there is no cell growing on the pillar. These pillars are expected to have zero deflection in an ideal case. However, there is considerable deflection noticed from the fitting results of the image. Therefore the average deflection of these pillars at rest is regarded as systematic error, which is subtracted from the calculated deflection of all the pillars in the following analysis. Besides this system error that is not associated with any cells, Prof. James Hone's group also took the displacement error caused by optical distortions upon cell-pillar contact (lensing effect) into consideration[67]. To do this, they plated cells on ultrastiff PDMS pillars assuming the cells would not be able to deflect them. The apparent displacements of these pillars were obtained and found to mainly originate from optical lensing effect.

We chose to adopt the mythology used by Ladoux's group and compare our resolution with theirs. In our experiment, all pillars are tracked before cells are plated to establish a reference (zero force) position. After cells spread over the pillars, pillar positions are measured again. Displacement of pillars is obtained by subtracting these two positons of corresponding (same) pillar. Average pillar displacement in an area away from any cell is the spatial pillar localization precision, and is subtracted from the displacement of pillar which is covered by cell for cell force.

Table 4.1 Precision of PDMS pillar array based cell force sensor

Obj. Lens	Imaging Method Bright field (B) Fluorescent fibronectin (F) Quantum dots (Q)	Precision	Cell	Reference
60x/0.8 air	B or F	~50 nm	MDCK	60
40x/0.6 air	B	5 nm	MEF	68
60x/0.9 water	B or F	20~30 nm	3T3 fibroblast & MDCK	38
40x	F	~25 nm	HUVEC	54
	B or F	25~30 nm	MDCK	66
60x/0.9 water	F	20~30 nm	REF52 fibroblast	69
100x/1.4	F	~30 nm	mouse fibroblast	70
100x/1.4	F	30 nm	3T3 fibroblast & MCF-7	59
60x	F	200 nm	NIH/3T3 mouse fibroblast & BPASMC	71
63x/1.4	F	30 nm	NIH/3T3 mouse fibroblast	41
40× air	Q	150 nm	HASM & RASM	61
100x/1.4 oil	F	25 ± 9 nm	MEF	67

Precision affected by the thickness of media over the pillar

To investigate the pillar localization precision of our device, we first carry out a study on whether the thickness of media coverage on the pillar has an effect on precision. We see a difference in signal-to-contract ratio when the thickness varies. Similar to the method described in previous section, we first add 4 ml culture media and capture the reference image. For a quick test, we don't grow cells on the device. Instead, we manually rotate the device a little bit to introduce position disturbance, since in the real case with cells, the device can never be positioned in the exact same coordinates on the microscope stage as where it is before the cells are plated. We then take a second image as the "cell" image. We select the same area in both images and subtract fitted position of pillars in "cell" image from that of corresponding pillars in reference image after these two images are aligned. The result from subtraction is the apparent pillar displacement, and the mean of its histogram gives the position precision. Precision for 2 ml cell culture media coverage is obtained in the same way after 2 ml DMEM is aspirated from the petri dish. In Fig. 4.4, we could see better precision ~17 nm in case of 2 ml compared to ~25 nm in case of 4 ml, which is probably due to a higher signal-to-noise ratio. However, this difference is not significant because signal-to-noise ratio in both cases is high enough for an accurate fitting. We also want to point out that the precision calculated here is underestimated compared to the real case with cells since there might be extra position disturbance introduced to the pillars at rest during the handling of cells.

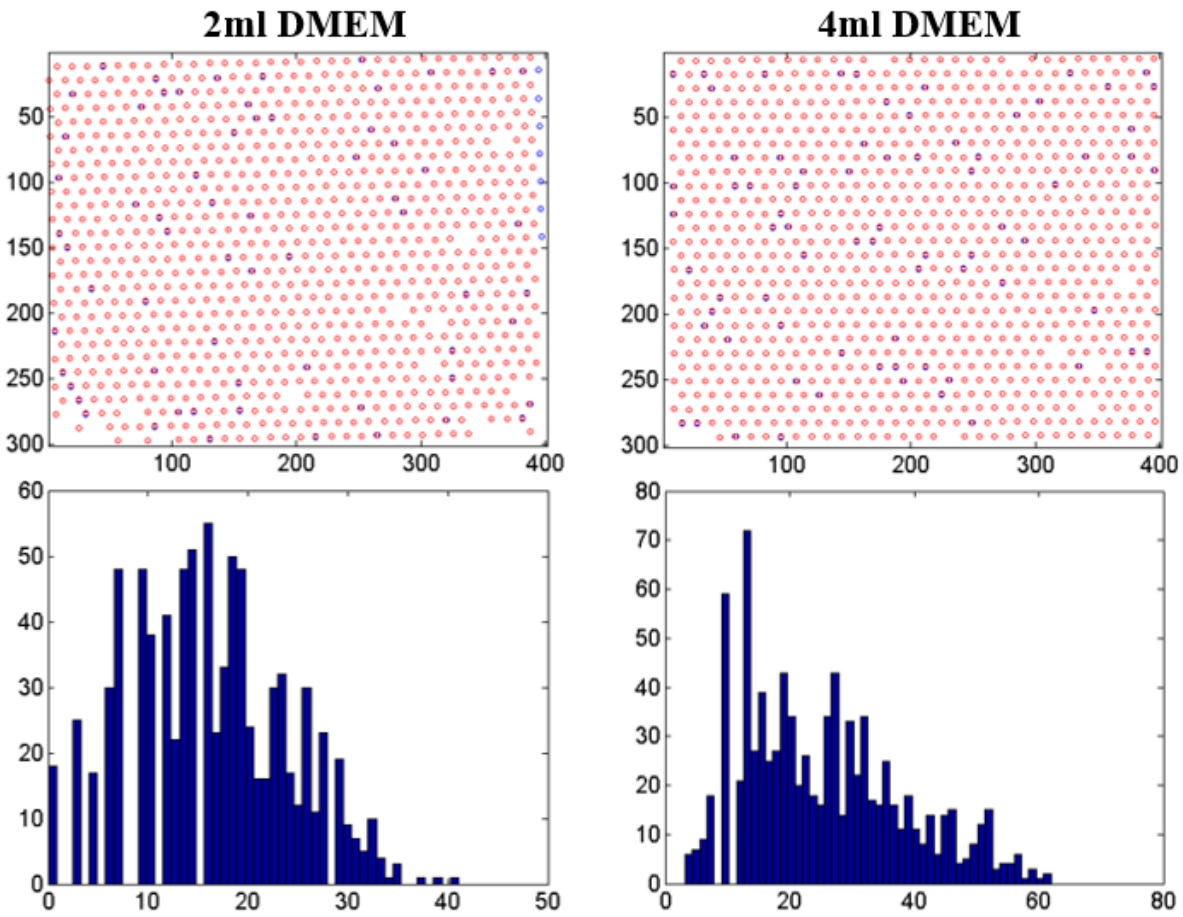

Figure 4.4 Precision of pillar localization affected by media thickness covered on top of pillars. Blue and red circles represent fitted pillar positions from reference and "cell" images. Mean value of the historiographic pillar displacement gives pillar position precision.

Precision in the real case with cells

For a more complete study of the precision, MDCK (Madin-Darby canine kidney, Sigma-Aldrich) epithelial cells are to be plated at subconfluent densities on fibronectin coated pillars. Before that, we take images of plasmonic PDMS micropillars as reference and then contact print the pillars with fibronectin (Sigma-Aldrich) at tip to help seeding of cells on the PDMS device. Detailed steps are listed as follows.

1) Make sure all pillars stand upward by critical point dryer;
2) Dispense 50 μg/ml fibronectin on flat stamping PDMS and let it absorb for 1hr;
3) Rinse stamping PDMS with PBS once;
4) Treat pillar with O_2 plasma at low power for 60~90 sec to make the surface hydrophilic;
5) Position stamping PDMS in contact with pillar device under light load for 20min;
6) Carefully peel away stamping PDMS and immerse device in 0.2 μl/ml Pluronic-127 for 15 min to avoid undesired attachment of cell to pillar sidewall;
7) Rinse with PBS 1~2 times;
8) Immerse device in a new petri dish filled with 5 ml DMEM culture media;
9) Plate few droplets of MDCK cells right on top of pillar area;
10) Cells are allowed to spread at least a day till well defined clusters of cells have grown;
11) Cells are fixed with 4% paraformaldehyde in PBS for 15 min.

Reference and cell images are both taken with 1 ml DMEM in petri dish for best signal-to-noise ratio without drying the sample during image capture. In dark field mode, the cells are actually hard to be seen. In a very last step, we stain the cells in Wheat Germ Agglutinin (WGA) Alexa Fluor® 594 (Life Technologies) for 20 min and take fluorescence image of cells. Cell image and the fluorescent image are stacked to evidence the correlation between pillar deflection and cell traction force. An area without cells is selected to obtain pillar localization precision as shown in Fig. 4.5. Mean value of pillar displacements in this area, ~30 nm, gives the spatial precision of pillar position.

The study of precision proves that we're able to monitor a larger area of cells in a less magnified optical system, 20x objective lens used here, without sacrificing the pillar localization precision.

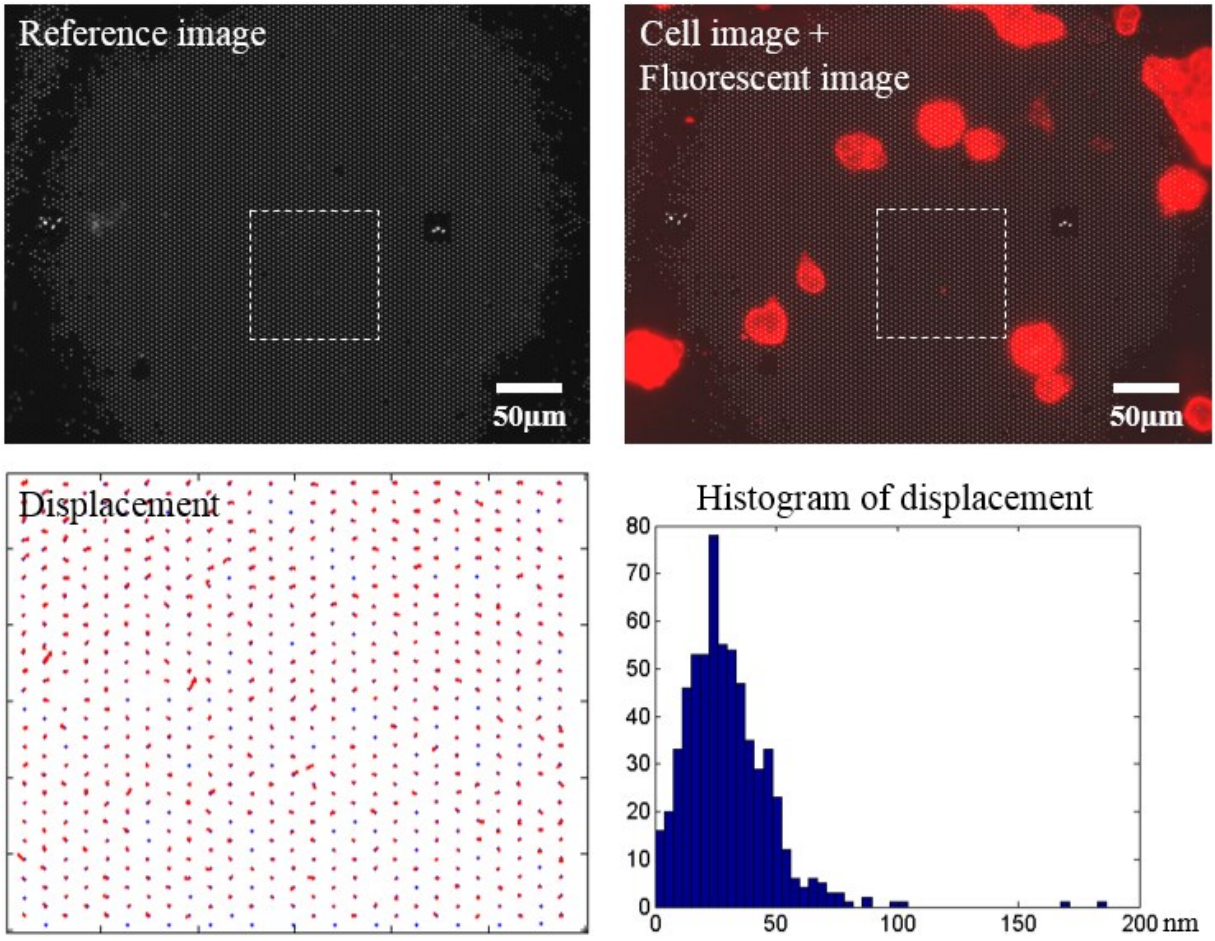

Figure 4.5 Pillar in the area enclosed by white dashed square is selected to calculate the precision. Blue dots and red arrows represent fitted pillar positions from cell image and the relative displacement of the pillars. Mean value of the historiographic pillar displacement gives pillar position precision.

4.4 Cell force measured by plasmonic PDMS pillar array

Once the displacement of pillar is obtained, the cell force can be deduced by simply multiplying the displacement by the stiffness of the elastic pillar with the assumption that the small displacement is in the linear regime. This proportional relation for a cylindrical PDMS pillar is formulated as

$$F = \frac{4}{3}\pi E \frac{r^4}{L^3} \Delta x \qquad (2)$$

where F is the traction force exerted by cell on underlying pillar, E is Young's modulus of PDMS, r and L is radius and height of the pillar, and Δx is the displacement bent by force F.

The pillars are anchored on the elastic substrate of the same material. When pillar bends, the base of pillar will warp too. This deformation of substrate will spread to surrounding area, and have an impact on the deflection of adjacent pillar. Thus the apparent deflection of a pillar should be attributed not only to the force that cell exerts on it, but also to the deflection of adjacent pillars. Ingmar Schoen et al. investigated on this substrate-mediated interplay between elastic pillars and found this interaction diminishes with third power of center-to-center distance[72, 73]. For most commonly used micropillar arrays, this relative error in the force determination is smaller than 5% and therefore can be neglected.

To obtain cell force, we have to align reference image and cell image first since they are not covering the exact same area of the pillar device when two images are taken. An iterative alignment is carried out until the accumulative pillar displacement in an area not covered by any cell reaches minimum. This criterion originates from the assumption that the positions of these unbent pillars from two images are supposed to be perfectly overlapping. The alignment includes

translational and rotational components. After reference and cell images are aligned, a direct subtraction of coordinates of corresponding pillar (cell deflected position minus original undeflected position) multiplied by the pillar stiffness is carried out to get the cell force exerted on each pillar.

Too soft PDMS pillars need to be avoided since too large deflection of the posts would lead to contact between adjacent pillars and then to under-estimated traction forces. This usually happens on the edge of a single cell or the cell cluster where the cell exerts largest traction force on the pillar.

Spatial distribution of forces applied by cell

Cell forces are calculated by home-developed MATLAB codes (Appendix A) and are usually represented by vectors drawn on each pillar whose length is proportional to the force magnitude. Fig. 4.6 gives the force map of MDCK cells growing on top of the pillar array. The largest force appears on the edge of cell clusters, usually implying the migration direction of the cells. The area without cell shows minimal pillar displacement.

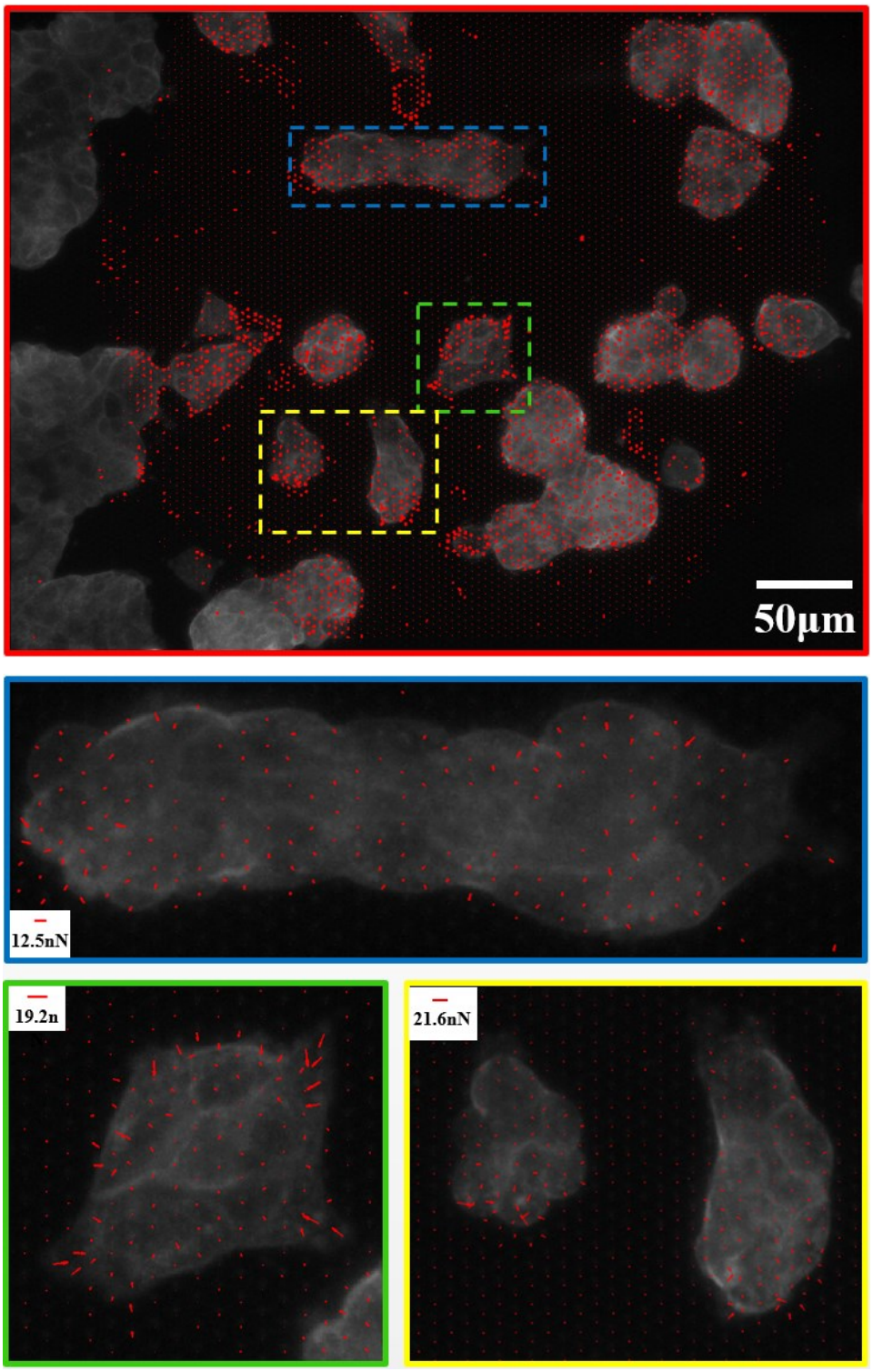

Figure 4.6 Cell force map imaged by a 20x objective lens.

4.5 Other potential functions of plasmonic PDMS pillar array

Photothermal delivery of molecules into live cells

Noble-metal nanostructures of different shape with unique photophysical properties have been used in photothermal treatment of cells of all kinds. In order to efficiently harvest the optical energy for sufficient thermal energy conversion, nanostructures with a typical size of tens nanometer to hundreds of nanometer are required. Depending on the size and density of cavitation bubbles induced by metal nanoparticles, photothermal treatments can be categorized into live cell delivery by opening small transient holes in membrane and cell therapy/ablation by fatally rupturing the membrane. Gold nanoparticles embedded in our PDMS micropillar array satisfy the size requirement and thus can be potentially used for photothermal treatment of cells growing on the pillar.

We first test damage threshold of gold nanoparticles embedded in PDMS pillar. Nanosecond laser pulses are sent into the microscope through back port and slightly focused by the objective lens to right cover its FOV. Laser energy measured before it enters the microscope is increased gradually till visible damage on gold nanoparticles is observed. The damage could result from evaporation of gold nanoparticles under too large laser energy or detachment of gold nanoparticles from pillar tip caused by shockwave and high-speed flows generated by cavitation bubbles. Fig. 4.7 shows no visible damage on gold nanoparticles when the laser energy is below 350 μJ. Severe damage can be noticed when laser energy is further increased to 500 μJ.

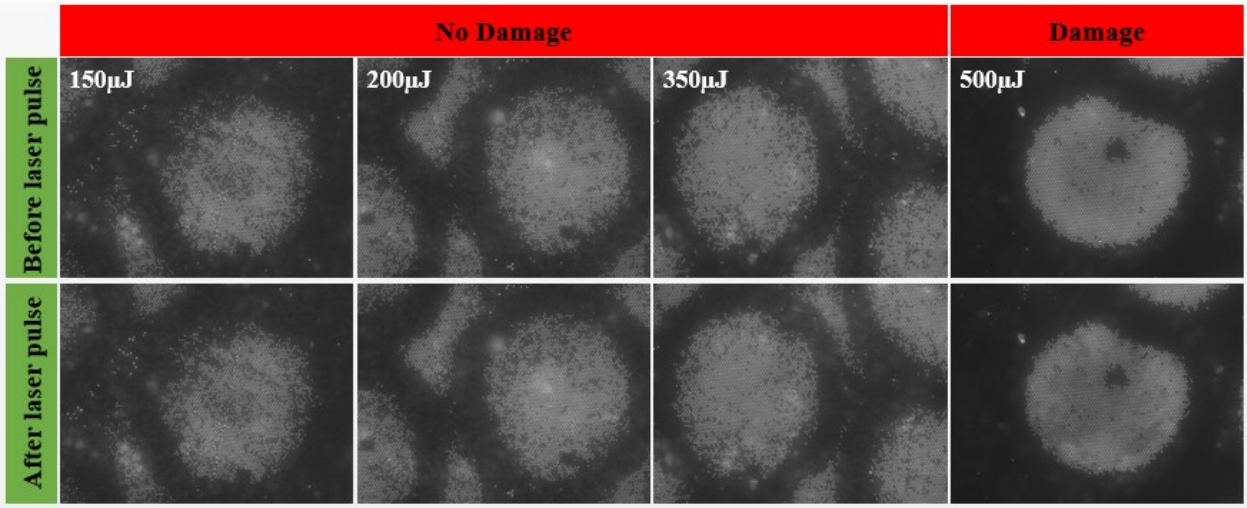

Figure 4.7 Damage threshold test on gold nanoparticles embedded in PDMS pillar immersed in culture media when triggered by nanosecond laser pulses. No visible damage shows up on gold nanoparticles when the laser energy is below 350 μJ. Severe damage can be noticed when laser energy is 500 μJ.

With the knowledge of a safe laser energy widow without damaging the gold nanoparticles, we try to deliver Calcein (Sigma-Aldrich) into HeLa cells growing on plasmonic PDMS pillar. The preliminary results show that the efficiency of molecular delivery into live cells strongly depends on the laser energy. This can be rationalized by the size of holes formed on cell membrane generated by fast expanding cavitation bubbles. In general, the efficiency increases with laser energy due to larger pores induced by larger cavitation bubbles, until the pores are too large to recover which will fatally destroy the cell. Fig. 4.8 shows Calcein uptake by cell under varied laser energy and corresponding cell viability as illustrated by Propidium Iodide (PI, Sigma-Aldrich). A control experiment is carried out on flat PDMS besides the pillar area. Only few cells show Calcein delivery, which is likely due to cavitation bubbles generated by gold residuals left on flat PDMS area during the surface gold removal step.

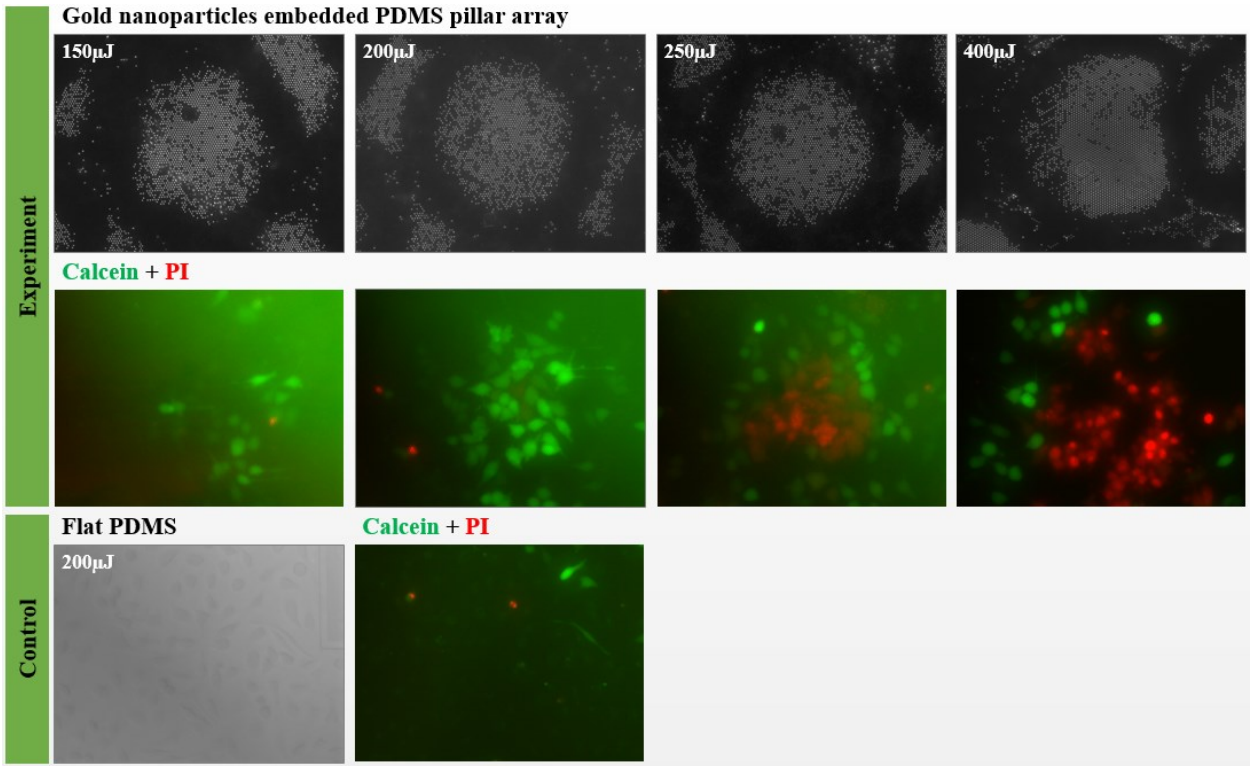

Figure 4.8 Photothermal delivery of Calcein into live Hela cells on the platform of plasmonic pillar array.

Chapter 5

Conclusion

We have demonstrated a near field photothermal printing method for rapid laser printing of gold micro and nanostructures, such as nanowires, microsquares, and nanospheres and other arbitrary patterns. It utilizes laser induced dewetting and self-organization processes guided by spatially shaped light patterns between a transparent phase shifting mask and a gold thin film to be printed. The rapid laser pulsing, metal dewetting, and shape evolution processes promise it a high speed printing technology for fabricating metallic nanostructures.

We also developed a novel large area plasmonic cell force sensor platform with superior force sensing accuracy. We have achieved 30 nm pillar position accuracy under a 20x objective lens with a FOV of 450 μm × 340 μm, an area more than 10 times larger than conventional micropillar array approaches. This high position accuracy comes from the strong plasmonic scattering signal of gold nanoparticles embedded in micropillars which provides strong signal-to-noise ratio and point-source-like image pattern for sub-pixel resolution tracing even under a low magnification objective lens. Furthermore, due to unique photophysical property of the

embedded gold nanoparticles in pillar tip, this platform shows the potential to be useful for biomolecule delivery into live cells by laser triggered cavitation bubbles.

APPENDIX A: MATLAB Codes

```
**********************************************************************
function main
clear all;
close all;
clc;
% Read Images
Iref = [];
Iref(:,:) = imread([num2str('7r') '.tif']);
resizer = [497,797;588,888];        % choose an area not covered by cell to align
[Ir] = Iref(resizer(1,1):resizer(1,2),resizer(2,1):resizer(2,2));
Icell = [];
Icell(:,:) = imread([num2str('7c') '.tif']);
resizec = [485,785;600,900];        % choose an area not covered by cell to align
[Ic] = Icell(resizec(1,1):resizec(1,2),resizec(2,1):resizec(2,2));
figure;
imshow(Ir, []);
figure;
imshow(Ic, []);
% Find peaks
[peakref] = peakfind(Ir,35000,4);       % unfitted peak
[peakcell] = peakfind(Ic,35000,4);
```

```
% restore coordinates in full image
peakref(:,2) = peakref(:,2) + resizer(1,1)-1;
peakref(:,3) = peakref(:,3) + resizer(2,1)-1;
peakcell(:,2) = peakcell(:,2) + resizec(1,1)-1;
peakcell(:,3) = peakcell(:,3) + resizec(2,1)-1;
% Gaussian fitting
[Maxref] = GaussFit(Iref,peakref,4,size(Iref));     %  fitted peak
[Maxcell] = GaussFit(Icell,peakcell,4,size(Icell));
Maxref(:,2) = Maxref(:,2) - (resizer(1,1)-1);
Maxref(:,3) = Maxref(:,3) - (resizer(2,1)-1);
Maxcell(:,2) = Maxcell(:,2) - (resizec(1,1)-1);
Maxcell(:,3) = Maxcell(:,3) - (resizec(2,1)-1);
figure;
plot(Maxref(:,3),Maxref(:,2),'o','MarkerSize',3)
hold on;
plot(Maxcell(:,3),Maxcell(:,2),'ro','MarkerSize',3)
set(gca,'YDir','reverse')
axis([1 size(Ir,2) 1 size(Ir,1)])
% Alignment
lr = length(Maxref(:,1));
origin = [0 0];
align0 = [-0.3, 0.3, -0.23, 0];
[align] = compsum(Maxcell, Maxref, align0, origin);    % find smallest displacement sum
```

```
[align] = compsumfine(Maxcell, Maxref, align, origin);
Maxref_precision = ROT(Maxref,align,lr,origin);
% plot displacement histogram for precision
Maxref = round(Maxref_precision*100)/100;
Maxcell = round(Maxcell*100)/100;
[DisHist] = Histogram(Maxcell, Maxref_precision);      % Displacement histogram
DisHist = DisHist * 6450 / 20;                  %  real displacement in [nm]
figure;
hist(DisHist,50);
set(gca,'fontsize',15);
% rotate whole image for cell force
 [peakref] = peakfind(Iref,35000,4);          % Find peaks
[peakcell] = peakfind(Icell,25000,4);
 [Maxref] = GaussFit(Iref,peakref,4,size(Iref));    % Gaussian fitting
[Maxcell] = GaussFit(Icell,peakcell,4,size(Icell));
lr = length(Maxref(:,1));
origin = [(resizer(1,1)-1) (resizer(2,1)-1)];
Maxref_align = ROT(Maxref,align,lr,origin);
Maxref_align(:,2) = Maxref_align(:,2) - 12;       % resizer(1,1) – resizec(1,1)
Maxref_align(:,3) = Maxref_align(:,3) + 12;       % resizer(2,1) – resizec(2,1)
Maxref = round(Maxref_align*100)/100;
Maxcell = round(Maxcell*100)/100;
% calculate cell force and plot
```

```
N = size(Maxref,1);
M = size(Maxcell,1);
Def = zeros(N,4);        % Deflection
for a = 1:M
   for b = 1:N
      r = sqrt((Maxcell(a,2)-Maxref_align(b,2))^2+(Maxcell(a,3)-Maxref_align(b,3))^2);
      if r<5
         Def(a,1) = Maxcell(a,2);
         Def(a,2) = Maxcell(a,3); % x-coordinate
         Def(a,3) = Maxcell(a,2) - Maxref_align(b,2); % y-deflection
         Def(a,4) = Maxcell(a,3) - Maxref_align(b,3); % x-deflection
      end
   end
end
figure;
imshow(Icell, []);
hold on;
quiver(Def(:,2),Def(:,1),Def(:,4),Def(:,3),0.5,'r');
set(gca,'YDir','reverse')
axis([1 size(Iref,2) 1 size(Iref,1)])
set(gca,'fontsize',15);
**********************************************************************
function out = peakfind(I,th,bd)
```

```
% Find peaks
[outresize] = pkfnd(I,th,bd);      * pkfnd is cited from ref 75.
Nr = size(outresize(:,1),1);
ptsr = zeros(Nr,3);
for a = 1:Nr
      c = outresize(a,1);
      r = outresize(a,2);
      ptsr(a,1) = I(r,c);
      ptsr(a,2) = r;    % row coordinates (y)
      ptsr(a,3) = c;    % column coordinates (x)
end
[out] = ptsr;
**********************************************************************
function Fitpts = GaussFit(I,pts,fs,sz)
% Gaussian Fit
N=size(pts,1);
Fitpts = zeros(N,3);
for a = 1:N
   v = pts(a,1);
   r = pts(a,2);
   c = pts(a,3);
   FitdataSize = min([fs/2,r-1,c-1,sz(1,1)-r,sz(1,2)-c])*2;
   [C,R] = meshgrid(-FitdataSize/2:FitdataSize/2);
```

```
    xdata = zeros(size(R,1),size(C,2),2);
    xdata(:,:,1) = R + r;  % row coordinates
    xdata(:,:,2) = C + c;  % column coordinates
    ydata = zeros(size(R,1),size(C,2));
    ydata = I((r-FitdataSize/2):(r+FitdataSize/2),(c-FitdataSize/2):(c+FitdataSize/2));
    x0 = [v,r,1,c,1];        % [Amplitude, r0, sigmar, c0, sigmac]
    [x,resnorm,residual,exitflag] = lsqcurvefit(@GaussFun,x0,xdata,ydata);
    % exitflag 3 :  Change in RESNORM too small.
    Fitpts(a,1) = x(1);
    Fitpts(a,2) = x(2);      % row (y)
    Fitpts(a,3) = x(4);      % column (x)
end
*********************************************************************
function F = GaussFunFit(x,xdata)
 F = x(1)*exp(-((xdata(:,:,1)-x(2)).^2/(2*x(3)^2) + (xdata(:,:,2)-x(4)).^2/(2*x(5)^2)));
*********************************************************************
function [ref] = compsum(Maxcell, Maxref, align0, origin)
lr = length(Maxref(:,1));
lc = length(Maxcell(:,1));
ref = [0, 0, 0, 1000];                    % inital sum 1000
for a = 1:20                              % 0.75~1.25 align0(1)
    y = align0(1) - 0.5 + a * 0.05;
    for b = 1:20
```

```
x = align0(2) - 0.5 + a * 0.05;
for c = 1:20
   r = align0(3) - 0.05 + c * 0.005;
   align = [y,x,r,0];
   Maxref_rot = ROT(Maxref,align,lr,origin);
   for d = 1:lc
      min = 5;
      for e = 1:lr
         dd = sqrt((Maxref_rot(e,2)-Maxcell(d,2))^2+(Maxref_rot(e,3)-
Maxcell(d,3))^2);
         if dd<min
            min = dd;
         end
      end
      if min == 5
         min = 0;                    % error
      end
      align(4) = align(4) + min;          % sum of displacement
   end
   if align(4)<ref(4)
      ref = align;
   end
end
```

```
    end
end
**********************************************************************
function out = ROT(I,align,lg,origin)
for i = 1:lg
    alpha = atan((I(i,2)- origin(1,1))/(I(i,3)-origin(1,2)));
    out(i,2) = (I(i,2)-origin(1,1)) / sin(alpha) * sin(alpha + align(1,3)*pi/180) + origin(1,1);
    out(i,3) = (I(i,3)-origin(1,2)) / cos(alpha) * cos(alpha + align(1,3)*pi/180) + origin(1,2);
end
out(:,2) = out(:,2) + align(1,1);
out(:,3) = out(:,3) + align(1,2);
out(:,1) = I(:,1);
**********************************************************************
function out = Histogram(Maxcell, Maxref)
lc = length(Maxcell(:,1));
lr = length(Maxref(:,1));
out = zeros(lr,1);
for a = 1:lr
    min = 5;
    for b = 1:lc
        r = sqrt((Maxcell(b,2)-Maxref(a,2))^2+(Maxcell(b,3)-Maxref(a,3))^2);
        if r<min
            min = r;
```

```
        end
    end
    if min == 5
        min = 0;
    end
    out(a) = min;
end
```

REFERENCES

1. K. Nishioka and S. Horita, “Periodic arrays of submicron Si and Ni dots on SiO_2 fabricated using linearly polarized Nd:YAG pulsed laser”, Appl. Phys. A, 2008, Vol. 91, 235 – 240.
2. Y. Kaganovskii,a H. Vladomirsky, and M. Rosenbluh, “Periodic lines and holes produced in thin Au films by pulsed laser irradiation”, J. Appl. Phys. 2006, Vol. 100, 044317.
3. Y. Kaganovskii, H. Vladomirsky, and M. Rosenbluh, “Fabrication of periodic structures in thin metal films by pulsed laser irradiation”, J. Nanophotonics, 2007, Vol. 1, 011690.
4. W. Huang, W. Qian, and M. A. El-Sayeda, “Photothermal reshaping of prismatic Au nanoparticles in periodic monolayer arrays by femtosecond laser pulses”, J. Appl. Phys. 2005, Vol. 98, 114301.
5. Q. Xia and S. Y. Chou, “The fabrication of periodic metal nanodot arrays through pulsed laser melting induced fragmentation of metal nanogratings”, Nanotechnolog, 2009, Vol. 20, 285310.
6. C. Wang, Q. Xia, W. Li, Z. Fu, K. J. Morton, and S. Y. Chou, “Fabrication of a 60-nm-diameter perfectly round metal-dot array over a large area on a plastic substrate using nanoimprint lithography and self-perfection by liquefaction”, Small 2010, Vol. 6 No. 11, 1242 – 1247.
7. M. Law, L. E. Greene, J. C. Johnson, R. Saykally, and P. Yang, “Nanowire dye-sensitized solar cells”, Nature Materials, 2005, Vol. 4, 455 – 459.
8. M. Righini, A. S. Zelenina, C. Girard, and R. Quidant, “Parallel and selective trapping in a patterned plasmonic landscape”, Nature Physics, 2007, Vol. 3, 477 – 480.

9. E. Laux, C. Genet, T. Skauli, and T. W. Ebbesen, “Plasmonic photon sorters for spectral and polarimetric imaging”, Nature Photonics, 2008, Vol. 2, 161 – 164.
10. T. H. Wu, S. Kalim, C. Callahan, M. A. Teitell, and P. Y. Chiou, “Image patterned molecular delivery into live cells using gold particle coated substrates”, Opt. Express, 2010, Vol. 18, 938 – 946.
11. J. Kim, S. Park, J. E. Lee, S. M. Jin, J. H. Lee, I. S. Lee, I. Yang, J. S. Kim, S. K. Kim, M. H. Cho, and T. Hyeon, “Designed fabrication of multifunctional magnetic gold nanoshells and their application to magnetic resonance imaging and photothermal therapy”, Angewandte Chemie, 2006, Vol. 118 No. 46, 7918 – 7922.
12. C. Sönnichsen, B. M. Reinhard, J. Liphardt, and A. P. Alivisatos, “A molecular ruler based on plasmon coupling of single gold and silver nanoparticles”, Nature Biotechnology, 2005, Vol. 23, 741 – 745.
13. C. M. Cobley, S. E. Skrabalak, D. J. Campbell, and Y. Xia, “Shape-controlled synthesis of silver nanoparticles for plasmonic and sensing applications”, Plasmonics, Vol. 4, 171 – 179.
14. J. Alegret, T. Rindzevicius, T. Pakizeh, Y. Alaverdyan, L. Gunnarsson, and M. Kall, “Plasmonic properties of silver trimers with trigonal symmetry fabricated by electron-beam lithography”, J. Phys. Chem. C, 2008. Vol. 112 No. 37, 14313 – 14317.
15. B. Cui, C. Keimel, and S. Y. Chou, “Ultrafast direct imprinting of nanostructures in metals by pulsed laser melting”, Nanotechnology, 2010, Vol. 21, 045303.
16. M. Bechelany, X. Maeder, J. Riesterer, J. Hankache, D. Lerose, S. Christiansen, J. Michler, and L. Philippe, “Synthesis mechanisms of organized gold nanoparticles:

Influence of annealing temperature and atmosphere", Cryst. Growth Des, 2010, Vol. 10 No. 2, 587 – 596.

17. C. Mu, J. P. Zhang, and D. Xu, "Au nanoparticle arrays with tunable particle gaps by template-assisted electroless deposition for high performance surface-enhanced Raman scattering", Nanotechnology, 2010, Vol. 21 No. 1, 015604.
18. A. Habenicht, M. Olapinski, F. Burmeister,P. Leiderer and J. Boneberg, "Jumping nanodroplets", Science, 2005, 309, 2043 – 2045.
19. D. A. Willis and V. Grosu, "Microdroplet deposition by laser-induced forward transfer", Appl. Phys. Lett., 2005, Vol 86, Issue 24, 244103
20. L. Yang, C. Wang, X. Ni, Z. Wang, W. Jia and L. Chai, "Microdroplet deposition of copper film by femtosecond laser-induced forward transfer", Appl. Phys. Lett., 2006, Vol 89, Issue 16, 161110.
21. A. I. Kuznetsov, A. B. Evlyukhin, C. Reinhardt, A. Seidel, R. Kiyan, W. Cheng, A. Ovsianikov, and B. N. Chichkov, "Laser-induced transfer of metallic nanodroplets for plasmonics and metamaterial applications", J. Opt. Soc. Am. B, Vol. 26, No. 12, B130 – B138.
22. V. Sametoglu, V. T. K. Sauer, and Y. Y. Tsui, "Production of 70-nm Cr dots by laser-induced forward transfer", Optics Express, 2013, Vol. 21, No. 15, 18525 – 18531.
23. U. Zywietz, C. Reinhardt, A. B. Evlyukhin, T. Birr, and B. N. Chichkov, "Generation and patterning of Si nanoparticles by femtosecond laser pulses", Appl Phys A, 2014, Vol. 114, 45 – 50.

24. A. Narazaki, R. Kurosaki, T. Sato, and H. Niino, “On-demand patterning of Indium Tin oxide microdots by laser-induced dot transfer”, Applied Physics Express, 2013, Vol. 6, No. 9, 092601.

25. P. Serra, M. Colina, J. M. Fernández-Pradas, L. Sevilla and J. L. Morenza, “Preparation of functional DNA microarrays through laser-induced forward transfer”, Appl. Phys. Lett., 2004, Vol. 85, No. 9, 1639 – 1641.

26. A. I. Kuznetsov, R. Kiyan, and B. N. Chichkov, “Laser fabrication of 2D and 3D metal nanoparticle structures and arrays”, Optics Express, 2010, Vol. 18, No. 20, 21198 – 21203.

27. W. T. Chen, M. L. Tseng, C. Y. Liao, P. C. Wu, S. Sun, Y. Huang, C. M. Chang, C. H. Lu, L. Zhou, D. Huang, A. Q. Liu and D. P. Tsai, “Fabrication of three-dimensional plasmonic cavity by femtosecond laser-induced forward transfer”, OPTICS EXPRESS, 2013, Vol. 21, No. 1, 618 – 625.

28. A. Narazaki, T. Sato, R. Kurosaki, Y. Kawaguchi, and H. Niino, “Nano- and microdot array formation of $FeSi_2$ by nanosecond excimer laser-induced forward transfer”, 2008, Appl. Phys. Express, Vol. 1, No. 5, 057001.

29. A.I. Kuznetsov, J. Koch, and B. N. Chichkov, “Laser-induced backward transfer of gold nanodroplets”, Optics Express, 2009, Vol. 17, No. 21, 18820 – 18825.

30. V. Sametoglu, V. T. K. Sauer, and Y. Y. Tsui, “Production of 70-nm Cr dots by laser-induced forward transfer”, Optics Express, 2013, Vol. 21, No. 15, 18525 – 18531.

31. A. Narazaki, T. Sato, R. Kurosaki, Y. Kawaguchi, and H. Niino, “Nano- and microdot array formation by laser-induced dot transfer”, Applied Surface Science, 2009, Vol. 255, Issue 24, 9703 – 9706.

32. L. Landström, J. Klimstein, G. Schrems, K. Piglmayer, and D. Bäuerle, “Single-step patterning and the fabrication of contact masks by laser-induced forward transfer”, Appl. Phys. A, 2004, Vol. 78, Issue 4, 537 – 538.
33. A. I. Kuznetsov, A. B. Evlyukhin, M. R. Gonc-alves, C. Reinhardt, A. Koroleva, M. L. Arnedillo, R. Kiyan, O. Marti, and B. N. Chichkov, “Laser fabrication of large-scale nanoparticle arrays for sensing applications”, 2011, ASC Nano, Vol. 5, No. 6, 4843 – 4849.
34. V. P. Veiko, and V. I. Konov, “Fundamentals of laser-assisted micro- and nanotechnologies”, 2014, Springer Series in Materials Science, Vol. 195, 107.
35. J. Thomas, R. Bernard, J. T. Thomas, K. Alti, S. Chidangil, S. Kumari, A. Khare, and D. Mathur, “Femtosecond laser induced forward transfer of indium thin films”, Laser and Particle Beams, 2014, Vol. 32, Issue 1, 55 – 61.
36. V Kotaidis, and A Plech, “Cavitation dynamics on the nanoscale”. Appl. Phys. Lett. 2005, Vol. 87, 213102.
37. E. B. Dickerson, E. C. Dreaden, X. Huang, I. H. El-Sayed, H. Chu, S. Pushpanketh, J. F. McDonald, and M. A. El-Sayed, “Gold nanorod assisted near-infrared plasmonic photothermal therapy (PPTT) of squamous cell carcinoma in mice”, Cancer Letters, 2008, Vol. 269, 57 – 66.
38. M. Ghibaudo, A. Saez, L. Trichet, A. Xayaphoummine, J. Browaeys, P. Silberzan, A. Buguin and B. Ladoux, “Traction forces and rigidity sensing regulate cell functions”, Soft Matter, 2008, Vol. 4, 1836 – 1843.

39. J. Fu, Y. Wang, M. T. Yang, R. A. Desai, X. Yu, Z. Liu & C. S. Chen, "Mechanical regulation of cell function with geometrically modulated elastomeric substrates", Nature methods, 2010, Vol .7, No. 9, 733 – 736.

40. A. Saez, M. Ghibaudo, A. Buguin, P. Silberzan, and B. Ladoux, "Rigidity-driven growth and migration of epithelial cells on microstructured anisotropic substrates", PNAS, 2007, Vol. 104, No. 20, 8281 – 8286.

41. M. T. Yang, N. J. Sniadecki, and C. S. Chen, "Geometric considerations of micro- to nanoscale elastomeric post arrays to study cellular traction forces", Adv. Mater. 2007, 19, 3119 – 3123.

42. M. K. Cheezum, W. F. Walker, and W. H. Guilford, "Quantitative comparison of algorithms for tracking single fluorescent particles", Biophys J., 2001, Vol. 81, No. 4, 2378 – 2388.

43. S. P. Lacour, J. Jones, Z. Suo, and S.Wagner, "Design and performance of thin metal film interconnects for skin-like electronic circuits", Electron Device Letters, 2004, Vol. 25, No. 4, 179 – 181.

44. J. Y. Baek, G. H. Kwon, J. Y. Kim, J. H. Cho, S. H. Lee, K. Sun, and S. H. Lee, "Stable deposition and patterning of metal layers on the PDMS substrate and characterization for the development of the flexible and implantable micro electrode", Solid State Phenomena, 2007, Vol. 124-126, 165 – 168.

45. J. N Patel, B. Kaminska, B. L. Gray and B. D. Gates, "A sacrificial SU-8 mask for direct metallization on PDMS", J. Micromech. Microeng., 2009, Vol. 19, No. 11, 115014.

46. K. Huang, S. Sattar, J. F. Zhong, C. Chou, H. Tsai, and P. Chiou, “Electrodes for microfluidic integrated optoelectronic tweezers”, Advances in OptoElectronics, 2011, Vol. 2011, 375451.

47. K. J. Lee, K. A. Fosser, and R. G. Nuzzo, “Fabrication of stable metallic patterns embedded in poly(dimethylsiloxane) and model applications in non-planar electronic and Lab-on-a-Chip device patterning”, Adv. Funct. Mater. 2005, Vol. 15, No. 4, 557 – 566.

48. K. S. Lim, W. Chang, Y. Koo and R. Bashir, “Reliable fabrication method of transferable micron scale metal pattern for poly(dimethylsiloxane) metallization”, Lab Chip, 2006, Vol. 6, No. 4, 578 – 580.

49. G. Lu, H. Li, and H. Zhang, “Gold-nanoparticle-embedded polydimethylsiloxane elastomers for highly sensitive raman detection”, Small, 2012, Vol. 8, No. 9, 1336 – 1340.

50. C. Chen and Y. Lee, “Fabrication of arrayed metallic nano-particles on a flexible substrate for inducing localized surface plasmon resonance”, Optics Express, 2013, Vol. 21, No. 3, 3265 – 3287.

51. H. Schmid, H. Wolf, R. Allenspach, H. Riel, S. Karg, B. Michel, and E. Delamarche, “Preparation of metallic films on elastomeric stamps and their application for contact processing and contact printing”, Adv. Funct. Mater., 2003, Vol. 13, Issue 2, 145 – 153.

52. R. McBeath, D. M. Pirone, C. M. Nelson, K. Bhadriraju, and C. S. Chen, “Cell shape, cytoskeletal tension, and RhoA regulate stem cell lineage commitment”, Dvelopmental Cell, 2004, Vol. 6, 483 – 495.

53. X. Trepat, M. R.Wasserman, T. E. Angelini, E. Millet, D. A.Weitz, J. P. Butler, and J, J. Fredberg, “Physical forces during collective cell migration”, Nature Physics, 2009, Vol. 5, 426 – 430.

54. A. Rabodzey, P. Alcaide, F. W. Luscinskas, and B. Ladoux, “Mechanical forces induced by the transendothelial migration of human neutrophils”, Biophysical Journal, 2008, Vol. 95, No. 3, 1428 – 1438.

55. K. NoelDahl, E. A. Booth-Gauthier, and B. Ladoux, “In the middle of it all: mutual mechanical regulation between the nucleus and the cytoskeleton”, J. Biomechanics, 2010, Vol. 43, No. 1, 2 – 8.

56. Z. Liua, J. L. Tanb, D. M. Cohena, M. T. Yang, N. J. Sniadecki, S. A. Ruiz, C. M. Nelson, and C. S. Chen, “Mechanical tugging force regulates the size of cell–cell junctions”, PNAS, 2010, Vol. 107, No. 22, 9944 – 9949.

57. Y. Sun, L. G. Villa-Diaz, R. H. W. Lam, W. Chen, P. H. Krebsbach, J. Fu, “Mechanics regulates fate decisions of human embryonic stem cells”, PLoS ONE, 2012, Vol. 7, No. 5, e37178.

58. A. Brugués, E. Anon, V. Conte, J. H. Veldhuis, M. Gupta, J. Colombelli, J. J. Muñoz, G.W. Brodland, B. Ladoux, and X. Trepat, “Forces driving epithelial wound healing”, Nature Physics, 2014, Vol. 10, 683 – 690.

59. H. Hoorn, R. Harkes, E. M. Spiesz, C. Storm, D. Noort, B.t Ladoux, and T. Schmidt, “The nanoscale architecture of force-bearing focal adhesions”, Nano Lett., 2014, Vol. 14, 4257 – 4262.

60. O.Roure, A. Saez, A. Buguin, R. H. Austin, P. Chavrier, P. Siberzan, and B. Ladoux, “Force mapping in epithelial cell migration”, PNAS, 2005, Vol. 102, No. 7, 2390 – 2395.

61. K. A. Addae-Mensah, N. J. Kassebaum, M. J. Bowers II, R. S. Reiserer, S. J. Rosenthal, P. E. Moore, and J. P. Wikswo, “A flexible, quantum dot-labeled cantilever post array for studying cellular microforces”, Sensors and Actuators A, 2007, Vol. 136, 385 – 397.

62. http://zeiss-campus.magnet.fsu.edu/articles/basics/resolution.html

63. K. A. Lidke, B. Rieger, T. M. Jovin, and R. Heintzmann, "Superresolution by localization of quantum dots using blinking statistics", Optics Express, 2005, Vol. 13, No. 18, 7052 - 7062.

64. R. E. Thompson, D. R. Larson, and W. W. Webb, "Precise nanometer localization analysis for individual fluorescent probes", Biophysical Journal, 2002, Vol. 82, 2775 – 2783.

65. J. C. Crocker and D. G. Grier, "Methods of digital video microscopy for colloidal studies", Journal of Colloid and Interface Science, 1996, Vol. 179, 298 – 310.

66. A. Saez, E. Anon, M. Ghibaudo, O. du Roure, J.-M. Di Meglio, P. Hersen, P. Silberzan, A. Buguin, and B. Ladoux, "Traction forces exerted by epithelial cell sheets", J. Phys.: Condens. Matter, 2010, Vol. 22, 194119.

67. S. Ghassemi, G. Meacci, S. Liu, A. A. Gondarenko, A. Mathur, P. Roca-Cusachs, M. P. Sheetz, and James Hone, "Cells test substrate rigidity by local contractions on submicrometer pillars", PNAS, 2012, Vol. 109, No. 14, 5328 – 5333.

68. Y. Cai, N. Biais, G. Giannone, M. Tanase, G. Jiang, J. M. Hofman, C. H. Wiggins, P. Silberzan, A. Buguin, B. Ladoux, and M. P. Sheetz, "Nonmuscle myosin IIA-dependent force inhibits cell spreading and drives F-actin flow", Biophysical Journal, 2006, Vol. 91, 3907 – 3920.

69. L. Trichet, J. Le Digabel, R. J. Hawkins, S. R. K. Vedula, M. Gupta, C. Ribrault, P. Hersen, R. Voituriez, and B. Ladoux, "Evidence of a large-scale mechanosensing mechanism for cellular adaptation to substrate stiffness", PNAS, 2012, Vol. 109, No. 18, 6933 – 6938.

70. H. van Hoorn, E. M. Spiesz, C. Storm, D. van Noort, B. Ladoux, and T. Schmidt, “High-resolution fluorescence measurements correlated to cellular traction forces”, Biophysical Journal, 2013, Vol. 104, No. 2, 193a.
71. J. L. Tan, J. Tien, D. M. Pirone, D. S. Gray, K. Bhadriraju, and C. S. Chen, “Cells lying on a bed of microneedles: an approach to isolate mechanical force”, PNAS, 2003, Vol. 100, No. 4, 1484 – 1489.
72. I. Schoen, “Substrate-mediated crosstalk between elastic pillars”, Appl. Phys. Lett., 2010, Vol. 97, 023703.
73. I. Schoen, W. Hu, E. Klotzsch, and V. Vogel, “Probing cellular traction forces by micropillar arrays: contribution of substrate warping to pillar deflection”, Nano Lett., 2010, Vol. 10, 1823 – 1830.
74. http://www.mathworks.com/matlabcentral/fileexchange/15765-sptrack1-0/content/pkfnd.m